

SID 67-498

STUDY OF APOLLO WATER IMPACT  
FINAL REPORT

VOLUME 2  
DYNAMIC RESPONSE OF SHELLS OF REVOLUTION DURING  
VERTICAL IMPACT INTO WATER - NO INTERACTION

(Contract NAS9-4552, G.O. 5264)


May 1967

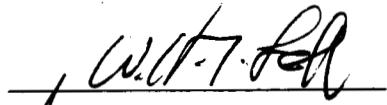


Prepared by

A. P. Cappelli  
J. P. D. Wilkinson  
(Authors)

Approved by

  
F. C. Hung  
Program Manager  
Structures and Materials

  
L. A. Harris  
Assistant Manager  
Science and Technology

NORTH AMERICAN AVIATION, INC.  
SPACE DIVISION

PRECEDING PAGE BLANK NOT FILMED.

## FOREWORD

This report was prepared by North American Aviation, Inc., Space Division, under NASA Contract NAS9-4552, for the National Aeronautics and Space Administration, Manned Space Flight Center, Houston, Texas, with Dr. F.C. Hung, Program Manager and Mr. P.P. Radkowski, Assistant Program Manager. This work was administered under the direction of Structural Mechanics Division, MSC, Houston, Texas with Dr. F. Stebbins as the technical monitor.

This report is presented in eleven volumes for convenience in handling and distribution. All volumes are unclassified.

The objective of the study was to develop methods and Fortran IV computer programs to determine by the techniques described below, the hydro-elastic response of representation of the structure of the Apollo Command Module immediately following impact on the water. The development of theory, methods and computer programs is presented as Task I Hydrodynamic Pressures, Task II Structural Response and Task III Hydroelastic Response Analysis.

Under Task I - Computing program to extend flexible sphere using the Spencer and Shiffman approach has been developed. Analytical formulation by Dr. Li using nonlinear hydrodynamic theory on structural portion is formulated. In order to cover a wide range of impact conditions, future extensions are necessary in the following items:

- a. Using linear hydrodynamic theory to include horizontal velocity and rotation.
- b. Nonlinear hydrodynamic theory to develop computing program on spherical portion and to develop nonlinear theory on toroidal and conic sections.

Under Task II - Computing program and User's Manual were developed for nonsymmetrical loading on unsymmetrical elastic shells. To fully develop the theory and methods to cover realistic Apollo configuration the following extensions are recommended:

- a. Modes of vibration and modal analysis.
- b. Extension to nonsymmetric short time impulses.

c. Linear buckling and elasto-plastic analysis

These technical extensions will not only be useful for Apollo and future Apollo growth configurations, but they will also be of value to other aeronautical and spacecraft programs.

The hydroelastic response of the flexible shell is obtained by the numerical solution of the combined hydrodynamic and shell equations. The results obtained herein are compared numerically with those derived by neglecting the interaction and applying rigid body pressures to the same elastic shell. The numerical results show that for an axially symmetric impact of the particular shell studied, the interaction between the shell and the fluid produces appreciable differences in the overall acceleration of the center of gravity of the shell, and in the distribution of the pressures and responses. However the maximum responses are within 15% of those produced when the interaction between the fluid and the shell is neglected. A brief summary of results is shown in the abstracts of individual volumes.

The volume number and authors are listed on the following page.

The contractor's designation for this report is SID 67-498.

## INDEX FOR FINAL REPORT DRAFT

### "Apollo Water Impact"

<u>Volume No.</u>	<u>Volume Title</u>	<u>Authors</u>
1	Hydrodynamic Analysis of Apollo Water Impact	T. Li and T. Sugimura
2	Dynamic Response of Shells of Revolution During Vertical Impact Into Water - No Interaction	A.P. Cappelli, and J.P.D. Wilkinson
3	Dynamic Response of Shells of Revolution During Vertical Impact Into Water - Hydroelastic Interaction	J.P.D. Wilkinson, A.P. Cappelli, R.N. Salzman
4	Comparison With Experiments	J.P.D. Wilkinson
5	User's Manual - No Interaction	J.P.D. Wilkinson
6	User's Manual - Interaction	J.P.D. Wilkinson and R.N. Salzman
7	Modification of Shell of Revolution Analysis	A.P. Cappelli and S.C. Furuike
8	Unsymmetric Shell of Revolution Analysis	A.P. Cappelli, T. Nishimoto, P.P. Radkowski and K.E. Pauley
9	Mode Shapes and Natural Frequencies Analysis	A.P. Cappelli
10	User's Manual for Modification of Shell of Revolution Analysis	A.P. Cappelli and S.C. Furuike
11	User's Manual for Unsymmetric Shell of Revolution Analysis	E. Carrion, S.C. Furuike and T. Nishimoto

PRECEDING PAGE BLANK NOT FILMED.

### ABSTRACT

A general method is developed for predicting the response of thin elastic shells of revolution subjected to arbitrary time-dependent loads. The method solves the dynamic shell equations by means of a definite-difference formulation in both space and time. As an application of the general numerical method, the response of blunt shells of revolution during a vertical impact into an incompressible fluid is studied. A formula is derived for the pressures on a rigid body of revolution during vertical impact. It is shown that the pressures are minimum at the impact point, and very large near the edge of the wetted surface of the body. These pressures are applied as a forcing function to a shell representing a typical re-entry vehicle. The numerical results show that the response is largest at the impact point, and the interaction of the flexible structure and the fluid may have an effect on the pressure distributions.

PRECEDING PAGE BLANK NOT FILMED.

CONTENTS

	Page
LIST OF ILLUSTRATIONS . . . . .	xi
NOMENCLATURE . . . . .	xiii
INTRODUCTION . . . . .	1
PRESSURE PROFILES . . . . .	3
DYNAMIC RESPONSE OF SHELLS OF REVOLUTION . . . . .	7
NUMERICAL ANALYSIS . . . . .	11
NUMERICAL RESULTS . . . . .	17
CONCLUSION . . . . .	21
ILLUSTRATIONS . . . . .	23
REFERENCES. . . . .	45
APPENDIX A - AUXILIARY RESULTS . . . . .	47

PRECEDING PAGE BLANK NOT FILMED.

# LIST OF ILLUSTRATIONS

Figure		Page
1	Model of Re-Entry Vehicle During Impact . . . . .	23
2	Acceleration of Center of Gravity of a Sphere During Impact into Water . . . . .	24
3	Pressure Profiles . . . . .	25
4	Shell Element . . . . .	26
5	Deflection W at Apex . . . . .	27
6	Meridional Bending Moment $M_{\xi}$ at Apex . . . . .	28
7	Meridional Membrane Force $N_{\xi}$ at Apex . . . . .	29
8	Velocity of Shell apex W . . . . .	30
9	Deflection W . . . . .	31
10	Meridional Stress at the Extreme Fiber . . . . .	32
11	Deflection W at Apex for Various Time Increments . . . . .	33
12	Meridional Bending Moment at Apex for Various Time Increments . . . . .	34
13	Reduction in Meridional Bending Moment at Apex Due To Reduced Edge Pressure . . . . .	35
14	Meridional Bending Moment $M_{\xi}$ . . . . .	36
15	Stress $\sigma_{\xi}$ On Outer Fiber at Apex . . . . .	37
16	Stereographic Pairs of the Rigid-Body Pressures Applied to Shell . . . . .	39
17	Average Pressure - Pull Scale Model . . . . .	41
18	Average Pressure - Quarter Scale Model . . . . .	42
19	Displacement W at Apex Illustrating Effect of Shell Flexibility . . . . .	43
20	Meridional Bending Moment $M_{\xi}$ at Apex Illustrating Effect of Shell Flexibility . . . . .	44

# NOMENCLATURE

## Pressure Profiles

$p$	pressure
$\rho$	mass density
$\phi$	velocity potential
$V_o$	initial rigid-body velocity
$V$	rigid-body velocity
$A$	rigid-body acceleration
$M$	total mass of shell
$m$	virtual mass of fluid
$\xi$	meridional shell coordinate
$\xi_F$	value of $\xi$ at edge of wetted surface
$R$	radius of curvature at impact point
$R(\xi)$	radius of curvature at $\xi$
$c$	maximum radius of wetted shell surface
$b$	depth of penetration
$r$	polar distance from impact point
$x$	vertical coordinate
$t$	time
$g$	acceleration due to gravity



## Shell Analysis

$a$	reference length
$s$	meridional coordinate
$\theta$	circumferential coordinate
$N_\xi, N_\theta, N_{\xi\theta}$	membrane forces
$M_\xi, M_\theta, M_{\xi\theta}$	bending moments
$\overline{N}_{\xi\theta}, \overline{M}_{\xi\theta}$	modified membrane shear and twisting moment
$U_\xi, V_\theta, W$	meridional, circumferential, and normal displacements
$q_\xi, q_\theta, q$	external loads per unit area
$t$	time variable
$\tau$	dimensionless time variable
$\xi$	dimensionless meridional coordinate
$m_0$	mass density
$E_0$	reference Young's modulus
$h$	shell thickness
$h_0$	reference shell thickness
$\sigma_0$	reference stress level
$t_\xi^{(n)}, t_\theta^{(n)}, t_{\xi\theta}^{(n)}$	Fourier coefficients of membrane forces
$m_\xi^{(n)}, m_\theta^{(n)}, m_{\xi\theta}^{(n)}$	Fourier coefficients of bending moments
$u_\xi^{(n)}, u_\theta^{(n)}, w^{(n)}$	Fourier coefficients of displacements
$p_\xi^{(n)}, p_\theta^{(n)}, p^{(n)}$	Fourier coefficients for loads
$n$	Fourier component

$\cdot$	$d( \ )/d\tau$
$'$	$d( \ )/d\xi$
$\bar{h}$	$h/h_0$
$j$	index denoting discrete time increment
$\epsilon$	dimensionless time increment
$i$	index denoting shell station point
$\Delta$	dimensionless meridional spatial increment
$N$	number of spatial stations
$z$	solution column matrix
$z_{i,0}, \bar{z}_{i,0}, \bar{\bar{z}}_{i,0}$	Fourier coefficient matrices of initial conditions

Other symbols are defined as they appear in the text, or are fully defined in Reference 2.

## INTRODUCTION

The design of elastic structures which impact into fluids requires a knowledge of the manner in which the structure responds to the impact forces, and a determination of the impact forces themselves. The purpose of this report is two-fold: first, to provide a means of calculating the pressure profiles which act on a shell of revolution during fluid impact, and second, to present a numerical method for the determination of the dynamic response of elastic shells of revolution subjected to arbitrary time-varying load distributions. The calculation of pressure profiles is restricted to those occurring during a vertical impact at a point on the shell where the rate of change of curvature is small in the neighborhood of the impact. The calculation of dynamic response, however, is quite general, and can be applied to any thin elastic shells of revolution within the framework of linear first-order shell theory.

The dynamic analysis of the elastic shell is based on Sanders' shell theory<sup>1</sup>, and involves an extension of the numerical procedure developed by Budiansky and Radkowski for the static analysis of shells<sup>2</sup>. An implicit numerical method of timewise integration is used in the solution of the dynamic problem. This implicit method was first used successfully by Houbolt in studying the response of aircraft to gust loads<sup>3</sup>. The Houbolt method was recently employed by Johnson and Greif in determining the dynamic response of a cylindrical shell<sup>4</sup>. The method presented here is a generalization of that used and suggested in Reference 4.

The Houbolt method features the use of backward difference expressions to represent the inertia terms in the dynamic shell equations. As shown by Johnson<sup>5</sup>, the method is numerically stable and thus offers an advantage over various other possible finite-difference methods. The finite-difference time increment, however, must be selected small enough to guarantee accurate results<sup>6</sup>. The spatial solution to the shell equations follows the procedure developed in Reference 2, and involves the expansion of the dependent variables in Fourier series, with the subsequent representation of the spatial derivatives in finite-difference form. A direct matrix elimination technique (Potters' method<sup>7</sup>) is used to solve the set of algebraic equations resulting from the finite-difference approximations to the reduced shell differential equations of motion.

The study of the impact of structures into fluids finds application in the problems associated with the slamming of ships in heavy seas, the water

entry of torpedoes, and the water landing of spacecraft. Surveys of the literature concerned with slamming and water impact have been made by Chu and Abramson<sup>8</sup> and by Szebehely and Ochi<sup>9</sup>. In the present problem, the maximum overall forces occur during a period when the motion of the fluid about the shell is adequately described by incompressible potential flow<sup>†</sup>.

The classical papers of von Kármán<sup>11</sup> and Wagner<sup>12</sup> have established methods of treating the two-dimensional impact of rigid V-wedges into an incompressible fluid. They showed how the concept of the virtual mass of the fluid could be used to advantage, and determined the pressures on rigid wedges by applying the known steady-state solutions for the flow about a flat plate to the unsteady hydrodynamic problem. The techniques developed for wedges also apply to the study of bodies of revolution. The impact of conical bodies has been investigated by Shiffman and Spencer<sup>13</sup>, who also gave the solution for the potential associated with the flow about a penetrating sphere<sup>14</sup>. Their solution for the sphere has been used by Korkegi<sup>15</sup> to predict the pressure history for an impacting sphere by considering the flow about a circular disc.

In this report, a modification of Korkegi's analysis is made for a rigid sphere. The pressures derived from this modification are applied as a forcing function to a shell of revolution. Numerical results are presented for the dynamic response of a shallow spherical shell during water impact. The shell structure is considered to be clamped below a heavier rigid mass (Figure 1) so that their combined mass simulates a typical re-entry vehicle. In this study, the effects of the hydroelastic interaction between the flexible shell and the fluid have been neglected. The forcing function is defined on the basis of a rigid-body analysis, and the response of the shell to this forcing function is studied. It is intended that these results will make possible an evaluation of the effect on the hydroelastic interaction which will form the subject-matter of Volume 3 of this report.

---

<sup>†</sup> In the present problem, the maximum forces are found to occur within the milli-second range. The effects of compressibility and air bubbles appear to predominate only in the microsecond range and are therefore neglected in this paper. These effects are discussed by Chuang<sup>10</sup> in connection with the impact of flat plates.

## PRESSURE PROFILES

According to incompressible potential theory, the flow of fluid around the shell is defined by a velocity potential  $\phi$  which satisfies Laplace's equation (see, for instance, Reference 16). The pressure in the fluid is related to  $\phi$  through Bernoulli's equation

$$p = \rho \left[ \frac{\partial \phi}{\partial t} - \frac{1}{2} (\nabla \phi)^2 + g x \right] \quad (1)$$

The fluid is displaced by the penetrating shell, and a thin sheath of fluid envelops the shell, as shown in Figure 1, where the free surface of the resulting splash is denoted by  $F_n$ . On this free surface the pressure must be equal to the ambient pressure. Following Shiffman and Spencer<sup>14</sup>, it will be assumed that the second term in Bernoulli's equation is small compared with the first, which means that the effect of the spray root is neglected, and the free surface remains plane during impact. The resulting planar surface is denoted in Figure 1 by  $F_p$ . It follows from Equation (1) that

$$\phi = 0 \text{ on } F_p \quad (2)$$

During the impact, the penetrating vehicle imparts some of its momentum to a virtual mass of fluid adjacent to it. To determine the magnitude of this virtual mass, the wetted surface of the penetrating shell is replaced by a flat disc of radius  $c$ . Consequently, the virtual mass  $m$  of the fluid is<sup>†</sup>

$$m = \frac{4}{3} \rho c^3 \quad (3)$$

The radius  $c$  of the wetted surface is related to the curvature of the shell  $R(\xi)$ , and to the depth of penetration  $b$ . If  $b/R \ll 1$ , then

$$2b = R - R(\xi_F)^2 \left( 1 - \sin^2 \xi_F \right) / R \quad (4)$$

---

<sup>†</sup> The virtual mass used here is half that given in Reference 16, p. 144, because only half of the disc is in contact with the fluid.

For a shell whose change in curvature is small in the neighborhood of the impact point,

$$R(\xi_F) \sim R \quad (5)$$

so that, approximately,

$$c = (2bR)^{1/2} \quad (6)$$

According to the principle of conservation of momentum, the instantaneous velocity  $V$  of the center of gravity of the vehicle is

$$V = \frac{db}{dt} = V_0 (1 + m/M)^{-1} \quad (7)$$

The distances  $c$  and  $b$  are approximated by\*\*

$$\begin{aligned} b &= V_0 t \\ c &= (2R V_0 t)^{1/2} \end{aligned} \quad (8)$$

Thus, the acceleration  $A$  of the center of gravity is given by

$$A = - \left( 4\sqrt{2} \rho V_0^{5/2} R^{3/2} t^{1/2} / M \right) (1 + \gamma)^{-2} \quad (9)$$

where

$$\gamma = 8\sqrt{2} \rho (R V_0 t)^{3/2} / 3M$$

The time at which the acceleration is a maximum is

$$t = \frac{1}{R V_0} \left( \frac{3M}{40\sqrt{2} \rho} \right)^{2/3} \quad (10)$$

The velocity potential on the surface of the disc at any time is given by (Reference 16, p. 144)

$$\phi = \frac{2}{\pi} c V \left( 1 - \frac{r^2}{c^2} \right)^{1/2} \quad (11)$$

---

\*\*Actually the depth of penetration may be obtained from Equation (7) in the parametric form

$$b \left[ 1 + 16\sqrt{2} \rho (Rb)^{3/2} / 15M \right] = V_0 t$$

The pressure on the surface of the disc (at  $x = 0$ ) is found from Equation (1) to be

$$p = \frac{\sqrt{2} \rho V_o^{3/2} R^{1/2} [1 - \gamma (2 - 3r^2/c^2)]}{\pi t^{1/2} (1 - r^2/c^2)^{1/2} (1+\gamma)^2} - \frac{\rho V_o^2}{2(1+\gamma)^2} \left[ 1 + \frac{4r^2}{2c^2} \left( 1 - \frac{r^2}{c^2} \right)^{-1} \right] \quad (12)$$

The second term on the right-hand side of Equation (12) arises from the retention of the term  $-\frac{1}{2} \rho (\nabla \phi)^2$  in Bernoulli's Equation (1).

In order to illustrate some typical numerical results, a study was made of the impact of a sphere of radius 175 inches and weight 10000 lbs. into water of density (62.5 lbs./cu. ft. In Figure 2 is shown the acceleration history of the center of gravity for various initial impact velocities. The maximum acceleration for  $V_o = 30$  fps. occurs at  $t = 9.5$  milliseconds after impact. In Figure 3, pressure profiles are presented for an initial impact velocity of 30 fps. They are calculated from Equation (12) while ignoring the second term on the right-hand side.

The pressures are minimum at the point of initial impact, and increase to an infinite peak at the edge of the wetted surface. If the second term in Equation (12) were to be retained, its effect would be small everywhere except at the edge of the wetted surface, where its singular term would be negative at  $r = c$ . Near this point the effect of the nonlinear free surface would modify any singularities occurring in the present linear hydrodynamic theory. Because the second term introduces a physically unrealistic negative pressure at the edge of the wetted surface, only the first term of Equation (12) will be used to predict the pressure profiles. It predicts the essential features of the experimentally observed profiles<sup>††</sup>. At the instant of impact, the present incompressible flow theory predicts that the pressure on the shell is infinite, although the total force is always finite. In practice, of course, the effects of compressibility and air bubbles will modify these extremely large pressures. It should also be noted that at some time  $t_n$  after the impact, the pressure given by Equation (12) may become negative near the impact point, presumably because at that time the assumptions of linearity

---

†† Experimental water impact studies have been carried out by S. Stubbs at the NASA Langley Research Center on a 1/4-scale rigid model of the Apollo Command Module, which has a spherical base. Except at the singularity, the pressure profiles of Equation (12) compare favorably with the unpublished data obtained during these impact tests.

are no longer valid. However,  $t_n$  always occurs appreciably after the time of the maximum rigid-body acceleration, when the maximum total forces act on the shell, and as will be shown later, it is not unreasonable to assume that the maximum stresses in the shell will have already been attained by this time.



## DYNAMIC RESPONSE OF SHELLS OF REVOLUTION

The determination of the dynamic response of shells of revolution involves an extension of the work of Budiansky and Radkowski<sup>2</sup> developed for the static analysis of shells. For convenience, the nomenclature used in Reference 2 will be adopted here unless otherwise noted. Furthermore, the coordinate system, sign convention, and force descriptions (see Figure 4) are given in Reference 2, and will not be repeated here in detail.

The equations of motion for a shell of revolution based on Sanders' theory<sup>1</sup> are given by

$$a \left[ \frac{\partial}{\partial \xi} (\rho N_{\xi}) + \frac{\partial}{\partial \theta} (\bar{N}_{\xi\theta}) - \rho' N_{\theta} \right] + \omega_{\xi} \left[ \frac{\partial}{\partial \xi} (\rho M_{\xi}) + \frac{\partial}{\partial \theta} (\bar{M}_{\xi\theta}) - \rho' M_{\theta} \right] + \frac{1}{2} (\omega_{\xi} - \omega_{\theta}) \frac{\partial}{\partial \theta} (\bar{M}_{\xi\theta}) + a^2 \rho q_{\xi} - \rho h E_0 \frac{\partial^2 U_{\xi}}{\partial \tau^2} = 0 \quad (13a)$$

$$a \left[ \frac{\partial}{\partial \theta} (N_{\theta}) + \frac{\partial}{\partial \xi} (\rho \bar{N}_{\xi\theta}) + \rho' \bar{N}_{\xi\theta} \right] + \omega_{\theta} \left[ \frac{\partial}{\partial \theta} (M_{\theta}) + \frac{\partial}{\partial \xi} (\rho \bar{M}_{\xi\theta}) + \rho' \bar{M}_{\xi\theta} \right] + \frac{\rho}{2} \frac{\partial}{\partial \xi} \left[ (\omega_{\theta} - \omega_{\xi}) \bar{M}_{\xi\theta} \right] + a^2 \rho q_{\theta} - \rho h E_0 \frac{\partial^2 U_{\theta}}{\partial \tau^2} = 0 \quad (13b)$$

$$\frac{\partial}{\partial \xi} \left[ \frac{\partial}{\partial \xi} (\rho M_{\xi}) + \frac{\partial}{\partial \theta} (\bar{M}_{\xi\theta}) - \rho' M_{\theta} \right] + \frac{1}{\rho} \frac{\partial}{\partial \theta} \left[ \frac{\partial}{\partial \theta} (M_{\theta}) + \frac{\partial}{\partial \xi} (\rho \bar{M}_{\xi\theta}) + \rho' \bar{M}_{\xi\theta} \right] - a \rho (\omega_{\xi} N_{\xi} + \omega_{\theta} N_{\theta}) + a^2 \rho q - \rho h E_0 \frac{\partial^2 W}{\partial \tau^2} = 0 \quad (13c)$$

where the nondimensional time and space variables  $\tau$  and  $\xi$  are related to the respective dimensional quantities  $t$  and  $s$  by the expressions

$$\tau = (E_0/m_0)^{1/2} t/a, \quad \xi = s/a \quad (14)$$

In these formulas,  $h$  is the shell thickness,  $m_0$  is the mass density,  $E_0$  is a reference Young's modulus, and  $a$  is a reference length. In Equation (13) the effects of transverse shear distortion have been neglected. In addition, viscous damping terms have been neglected but their inclusion presents no inherent difficulties (e.g., see Reference 17).

All variables in Equation (13) are now expanded in Fourier series in the circumferential variable  $\theta$  as follows:

$$\begin{Bmatrix} N_\xi \\ N_\theta \\ M_\xi \\ M_\theta \\ U_\xi \\ W \\ q_\xi \\ q \end{Bmatrix} = \sigma_0 h_0 \sum_{n=0}^{\infty} \begin{Bmatrix} t_\xi^{(n)} \\ t_\theta^{(n)} \\ \frac{h^2}{a} m_\xi^{(n)} \\ \frac{h^2}{a} m_\theta^{(n)} \\ \frac{a}{E_0 h_0} u_\xi^{(n)} \\ \frac{a}{E_0 h_0} w^{(n)} \\ \frac{1}{a} p_\xi^{(n)} \\ \frac{1}{a} p^{(n)} \end{Bmatrix} \cos n\theta \quad (15)$$

$$\begin{Bmatrix} \bar{N}_{\theta\xi} \\ \bar{M}_{\xi\theta} \\ U_\theta \\ q_\theta \end{Bmatrix} = \sigma_0 h_0 \sum_{n=1}^{\infty} \begin{Bmatrix} t_{\xi\theta}^{(n)} \\ \frac{h^2}{a} m_{\xi\theta}^{(n)} \\ \frac{a}{E_0 h_0} u_\theta^{(n)} \\ \frac{1}{a} p_\theta^{(n)} \end{Bmatrix} \sin n\theta$$

where  $\sigma_0$  is a reference stress level, and  $h_0$  is a reference thickness. The Fourier coefficients in the above expansions are functions of  $\xi$  and  $r$ . Substitution of the above Fourier series into Equation (13) permits the uncoupling of the shell equations into separate sets for each Fourier index ( $n$ ). For convenience, the superscript ( $n$ ) will be omitted from the equations that follow.

By expressing forces and moments in terms of the four variables  $u_\xi$ ,  $u_\theta$ ,  $w$ , and  $m_\xi$ , and by introducing an auxiliary moment-displacement equation as was done in Reference 2, the shell equations can now be written in the following form:

$$\begin{aligned} a_{11}u_\xi'' + a_{12}u_\xi' + a_{13}u_\xi + a_{14}u_\theta' + a_{15}u_\theta + a_{16}w' \\ + a_{17}w + a_{18}m_\xi' + a_{19}m_\xi - \bar{h}\ddot{u}_\xi = c_1 \end{aligned} \quad (16a)$$

$$\begin{aligned} a_{10}u_\xi' + a_{11}u_\xi + a_{12}u_\theta'' + a_{13}u_\theta' + a_{14}u_\theta + a_{15}w' \\ + a_{16}w' + a_{17}w + a_{18}m_\xi - \bar{h}\ddot{u}_\theta = c_2 \end{aligned} \quad (16b)$$

$$\begin{aligned} a_{19}u_\xi' + a_{20}u_\xi + a_{21}u_\theta'' + a_{22}u_\theta' + a_{23}u_\theta + a_{24}w' \\ + a_{25}w' + a_{26}w + a_{27}m_\xi' + a_{28}m_\xi + a_{29}m_\xi \\ - \bar{h}\ddot{w} = c_3 \end{aligned} \quad (16c)$$

$$\begin{aligned} a_{30}u_\xi' + a_{31}u_\xi + a_{32}u_\theta + a_{33}w' + a_{34}w' + a_{35}w \\ + a_{36}m_\xi = c_4 \end{aligned} \quad (16d)$$

where

$$\bar{h} = h/h_0 \quad (17)$$

The coefficients  $a_i$  are functions of the material and geometric properties of the shell and of the Fourier index  $n$ . The terms  $c_i$  are functions of the applied load. The quantities  $(a_1, a_2, \dots, a_{36}, c_1, c_2, c_3, c_4)$  are given in Appendix A of Reference 2. Differentiation with respect to  $\xi$  and  $\tau$  is denoted by primes and dots, respectively. Equation (16) may be written in the matrix form

$$Ez'' + Fz' + Gz = e + \ddot{D}z \quad (18)$$

where

$$z = \begin{bmatrix} u_\xi \\ u_\theta \\ w \\ m_\xi \end{bmatrix} \quad D = \begin{bmatrix} \bar{h} & 0 & 0 & 0 \\ 0 & \bar{h} & 0 & 0 \\ 0 & 0 & \bar{h} & 0 \\ 0 & 0 & 0 & 0 \end{bmatrix} \quad (19)$$

and the matrices E, F, G, and e are given by Equations (41) of Reference 2.

The boundary conditions can be written in nondimensional matrix form as

$$\Omega H z' + (\Lambda + \Omega J) z = \ell - \Omega f \quad (20)$$

where the matrices H, J, and f are given by Equation (51) of Reference 2. As explained by Budiansky and Radkowski<sup>2</sup>,  $\Omega$  and  $\Lambda$  are prescribed diagonal matrices, and  $\ell$  is a prescribed column matrix indicating the type of boundary condition under consideration<sup>††</sup>. For example, if  $u_\xi$  is known at the boundary, the first diagonal element of  $\Omega$  is zero, the first diagonal element of  $\Lambda$  is unity, and the first element of  $\ell$  is the prescribed value of  $u_\xi$ .

---

<sup>††</sup>A special modification in the above matrices is necessary when treating problems where the shell has a closed apex. Procedures for handling such singular points are discussed in References 18 and 19.

## NUMERICAL ANALYSIS

In this volume the differential equations (18) and (20) will be expressed in finite-difference form, and a numerical procedure for their solution will be presented.

Discrete values of the nondimensional space variable  $\xi$  are denoted by

$$\xi_i = i \Delta \quad i = 0, 1, 2, \dots, N \quad (21)$$

where the nondimensional space increment  $\Delta$  is defined as

$$\Delta = \bar{s}/a (N - 1)$$

Similarly, discrete values of the nondimensional time variable  $\tau$  are denoted by

$$\tau_j = j \epsilon \quad j = -2, -1, 0, 1, 2, \dots \quad (22)$$

where  $\epsilon$  is the nondimensional time increment. As will be seen later, the fictitious times  $\tau_{-1}$  and  $\tau_{-2}$  will be necessary in the description of the initial conditions. The difference formulas used to represent derivatives with respect to the spatial variable  $\xi$  (at any time  $\tau_j$  and position  $\xi_i$ ) are

$$\begin{aligned} z''_{i,j} &= (z_{i+1,j} - 2z_{i,j} + z_{i-1,j})/\Delta^2 \\ z'_{i,j} &= (z_{i+1,j} - z_{i-1,j})/2\Delta \end{aligned} \quad (23)$$

$$i = 1, 2, \dots, N-1$$

$$\begin{aligned} z'_{0,j} &= (z_{1,j} - z_{0,j})/\Delta \\ z'_{N,j} &= (z_{N,j} - z_{N-1,j})/\Delta \end{aligned} \quad (24)$$

In order to be consistent with Reference 2, simple backward and forward difference expressions are used above in treating boundary points. More accurate procedures involving the introduction of fictitious points are discussed in References 4 and 20. A computer program developed at S&ID, which yields the numerical results of this paper, takes advantage of such improved difference expressions at boundary points.

The Houbolt method features the use of an improved backward difference technique for the determination of the time derivatives. This method is based on fitting a third degree polynomial in  $\tau$  through four consecutive discrete temporal points. The general expression for the second derivative of  $z_i$  with respect to time is given by

$$\ddot{z}_{i,j} = (2z_{i,j} - 5z_{i,j-1} + 4z_{i,j-2} - z_{i,j-3})/\epsilon^2$$

$$j = 1, 2, \dots$$
(25)

It is important to note that the initial increments of calculation (at  $j = 1, 2$ ) in the above expression involve the evaluation of functions at negative values of time. These fictitious functions  $z_{i,-1}$ ,  $z_{i,-2}$  can be determined from the prescribed initial conditions of the problem  $z_{i,0}$ ,  $\dot{z}_{i,0}$ , and  $\ddot{z}_{i,0}$ . By utilizing the difference formulas suggested by Houbolt<sup>3</sup> to start the process, the following expressions can be obtained:

$$z_{i,-1} = \epsilon^2 z_{i,0} + 2z_{i,0} - z_{i,1}$$

$$z_{i,-2} = 6\epsilon^2 z_{i,0} + 6\epsilon \bar{z}_{i,0} + 9z_{i,0} - 8z_{i,1}$$
(26)

Here,  $z_{i,0}$ ,  $\bar{z}_{i,0}$  and  $\ddot{z}_{i,0}$  are column matrices representing the coefficients of the appropriate Fourier expansions for the dimensionless initial displacement, velocity, and acceleration conditions, respectively.

By using Equations (23-26) the differential equations (18) and boundary conditions (20) can be expressed by the set of algebraic equations

$$A_0 z_{1,j} + B_0 z_{0,j} = g_{0,j}$$

$$A_i z_{i+1,j} + B_i z_{i,j} + C_i z_{i-1,j} = g_{i,j}$$

$$B_N z_{N,j} + C_N z_{N-1,j} = g_{N,j} \quad (i = 1, 2, \dots, N-1)$$
(27)

Here

$$A_0 = \Omega_0 H_0 / \Delta_1$$

$$B_0 = \Lambda_0 + \Omega_0 \left[ J_0 - (H_0 / \Delta_1) \right]$$

$$g_{0,j} = \ell_{0,j} - \Omega_0 f_{0,j}$$
(28)

where the subscript 0 refers to the end conditions at  $s = 0$ , and

$$\begin{aligned} B_N &= \Lambda_N + \Omega_N \left[ J_N + (H_N/\Delta_p) \right] \\ C_N &= - (\Omega_N H_N / \Delta_p) \\ g_{N,j} &= \ell_{N,j} - \Omega_N f_{N,j} \end{aligned} \quad (29)$$

where the subscript N refers to the boundary conditions at  $s = \bar{s}$ . For  $i = 1, 2, \dots, N-1$ , the coefficients are given by

$$\begin{aligned} A_i &= (2E_i/\Delta) + F_i \\ B_i &= - (4E_i/\Delta) + 2\Delta (G_i - \alpha_j D_i / \epsilon^2) \\ C_i &= (2E_i/\Delta) - F_i \\ g_{i,j} &= 2\Delta e_{i,j} - \frac{2\Delta D_i}{\epsilon^2} \left[ \beta_j z_{i,j-1} + \delta_j z_{i,j-2} + \eta_j z_{i,j-3} + \bar{\alpha}_j \bar{z}_0 + \bar{\beta}_j \epsilon^2 z_0 \right] \end{aligned} \quad (30)$$

$$\begin{aligned} \alpha_1 &= 6, & \alpha_2 &= 2, & \alpha_j &= 2 \\ \beta_1 &= 6, & \beta_2 &= 4, & \beta_j &= 5 \\ \delta_1 &= 0, & \delta_2 &= -2, & \delta_j &= -4 \\ \eta_1 &= 0, & \eta_2 &= 0, & \eta_j &= 1 \\ \bar{\alpha}_1 &= 6, & \bar{\alpha}_2 &= 0, & \bar{\alpha}_j &= 0 \\ \bar{\beta}_1 &= 2, & \bar{\beta}_2 &= 1, & \bar{\beta}_j &= 0 \\ & & (j = 3, 4, \dots) \end{aligned} \quad (31)$$

Assuming that  $g_{i,j}$  is known, it is evident that the above equations (27) are of the same form as those treated in the static problem. The method used to solve these equations is a direct matrix elimination technique (Potters' method<sup>7</sup>) which is described in detail in Reference 2. The basic procedure involves relating  $z_{i,j}$  to  $z_{i+1,j}$  by expressions of the form

$$z_{i,j} = -P_i z_{i+1,j} + x_{i,j} \quad (i = 1, 2, \dots, N-1) \quad (32)$$

where

$$\begin{aligned}
 P_i &= \left[ B_i - C_i P_{i-1} \right]^{-1} A_i \\
 x_{i,j} &= \left[ B_i - C_i P_{i-1} \right]^{-1} \left[ g_{i,j} - C_i x_{i-1,j} \right] \\
 (i &= 2, 3, \dots, N-1)
 \end{aligned} \tag{33}$$

$$\begin{aligned}
 P_i &= \left[ B_0 C_1^{-1} B_1 - A_0 \right]^{-1} B_0 C_1^{-1} A_1 \\
 x_{1,j} &= \left[ B_0 C_1^{-1} B_1 - A_0 \right]^{-1} \left[ B_0 C_1^{-1} g_{1,j} - g_{0,j} \right]
 \end{aligned}$$

From Equations (32) and the last of Equation (27), the correct value of  $z_{N,j}$  can be calculated as follows:

$$z_{N,j} = \left[ B_N - C_N P_{N-1} \right]^{-1} \left[ g_{N,j} - C_N x_{N-1,j} \right] \tag{34}$$

All the remaining  $z_{i,j}$  are calculated in the reverse order using Equation (32) starting from the calculated value  $z_{N,j}$ . The computations involve only inversions of 4 x 4 matrices. Finally,  $z_{0,j}$  is given by

$$z_{0,j} = C_1^{-1} \left[ g_{1,j} - A_1 z_{2,j} - B_1 z_{1,j} \right] \tag{35}$$

It can be seen that  $g_{i,j}$  in Equation (30), and in turn in the solution  $z_{i,j}$ , depends on the previous solutions  $z_{i,j-1}$ ,  $z_{i,j-2}$ ,  $z_{i,j-3}$ . To start the process at  $j = 1$ ,  $g_{i,1}$  is determined from the known initial conditions, and the resulting equations are solved by Potters' method to give  $z_{i,1}$ . By using  $z_{i,1}$  and the initial conditions,  $g_{i,2}$  is computed, and the resulting equations are solved for  $z_{i,2}$ . The cycle is repeated to determine subsequent values of  $z_{i,j}$ .

It should be noted that the solutions  $z_{i,j}$  obtained above represent the shell response for a particular Fourier index  $n$ . For the general case of unsymmetric loads, the complete solution is obtained by performing the appropriate summation of the Fourier coefficients using the Fourier expansions described by Equations (15). As pointed out by Johnson and Greif<sup>4</sup>, the Houbolt method of solution for the dynamic response reduces to the static solution as  $\epsilon$  becomes unbounded.



The basic numerical method discussed above can easily be extended to shells with discontinuities and branch conditions by following the parallel development of Reference 2 for the case of the statics of shells. An analysis of this type can also consider problems in which the material and geometric properties of the shell are time-dependent. In such cases, the matrices  $A_i$ ,  $B_i$  and  $C_i$  in Equations (28), (29) and (30) must be recomputed at each time interval.

## NUMERICAL RESULTS

The dynamic shell analysis described in this report was programmed for solution on a digital computer (IBM 7094). The user's manual for the computer program is described in Volume 5 of this report. Numerical results are presented for a sample problem simulating the vertical impact of a typical re-entry vehicle during water impact.

The mathematical model considered is illustrated in Figure 1 with the shell structure being a shallow spherical shell of radius of curvature  $R = 175.6$  ins. and having an opening angle of  $19.53^\circ$ . For convenience, an axisymmetric problem is considered (i.e., the impact point coincides with the apex of the shell) and only the Fourier component corresponding to the index  $n = 0$  is required. The stiffness parameters were selected to be characteristic of sandwich or layer shell configuration which is typically used in re-entry shell structures. The extensional stiffness (b) and flexural stiffness (d) of the shell are both set equal to  $3.33 \times 10^6$  lbs./in., which corresponds to a sandwich shell having 0.05 in. steel facings and 1.95 in. honeycomb core. It should be recognized that this configuration was selected for illustrative purposes and that transverse shear distortion effects, although neglected in this analysis, may be significant for such a sandwich configuration. Other properties of the shell are as follows: Mass per unit surface area ( $m_0 h$ ) =  $9.7 \times 10^{-4}$  lbs sec<sup>2</sup>/in.<sup>3</sup>, Poisson's ratio  $\nu = 0.33$ , and modulus of elasticity  $E = 29.7 \times 10$  psi. Referring to Figure 1, the shell is considered rigidly clamped at its boundary to a heavier mass (simulated re-entry capsule) so that their combined weight is 10,000 lbs.

The pressure applied to the shell is given in Figure 3 for a vertical impact into water at an initial velocity of 30 fps. The pressure loading from the first term of Equation (12) is seen to contain a singularity at the edge of the wetted surface. This singularity is integrable, however, so that the force acting on the shell is finite, and the applied pressure at each station point is averaged over a complete spatial increment.

The response of the shell due to these applied rigid-body pressures is illustrated in Figure 5-16. In order to determine the peak response of the shell, calculations were made up to 15 milliseconds from the time of impact (see Figures 5-8). This time is well beyond the time of occurrence of the maximum acceleration of the center of gravity of the vehicle (9.5 ms.). The response quantities shown in Figure 5-8 represent the displacement  $W$ , meridional bending moment  $M_\xi$ , meridional membrane force  $N_\xi$ , and velocity

$\dot{W}$  at the apex of the shell, obtained by using a time increment  $\Delta t$  of .05 ms. Inspection of the results indicates that peak shell response occurs at approximately 2.2 ms. after the impact. This peak is experienced appreciably before the time when the maximum force acts on the shell at 9.5 ms. Three-dimensional plots of the displacement  $W$  and the meridional stresses  $\bar{\sigma}_\xi$  at the extreme fiber of the shell are plotted in Figures 9 and 10 versus time and meridional distance on the shell surface measured from the impact point. Peak shell stresses occur at the apex of the shell at 2.2 ms. after impact. However, maximum stresses at subsequent times tend to follow the movement of the edge of the wetted surface. Thus, at later times, maximum stresses may occur at points other than the apex.

Dotted curves on Figures 5 and 6 represent results obtained when the pressures are applied statically, i. e., when the inertia effects of the shell are neglected. These results are sometimes referred to as the static crawl response, and, as one might expect, the dynamic response oscillates about the static crawl curves.

In order to ascertain the effect of the shell flexibility on the response, calculations were also made for the case where the flexural stiffness was reduced by one-half. It was observed that the peak deflection  $W$  was about 40% larger, and the peak stress at the extreme fibers was 35.7% larger. The peak response occurred at 2.8 ms, showing that for a more flexible shell the peak response is delayed.

As discussed in Reference 4, the accuracy of the Houbolt method varies with the size of the time increment ( $\epsilon$ ) used. It has been estimated<sup>6</sup> that the time increment  $\epsilon$  should be smaller than 1/50th of the period of the particular mode of vibration in order that important output quantities in that mode are not significantly damped. In Figures 11 and 12 are presented results for apex displacement and bending moment, obtained by varying the time increment  $\Delta t$  between 0.01 ms. and 0.3 ms. The results of Figure 11 reveal that excellent convergence in the deflection  $W$  occurs when a time increment of 0.025 ms. is selected. As might be expected, convergence is slower for the bending moment  $M_\xi$  since this quantity is computed numerically from derivatives of the displacements. Since the results are not significantly damped for a time increment of 0.05 ms., in the interests of economy, this time increment was selected for the longer response curves of Figures 5 to 8. No appreciable variation was noticed in the results when the number of stations ( $N$ ) was varied between 60 and 120.

Experimental observations show that although peak pressures occur at the edge of the wetted surface, they are by no means infinite, as predicted by the present linear hydrodynamic analysis. In order to ascertain the effect of these infinite pressures on the shell response, a profile whose radius was

99% of the predicted radius was applied to the shell. Thus, the infinite peak was excluded from the forcing function. Results of Figure 13, using a time increment of 0.1 ms., show an 8.5% reduction in the peak bending moment. The implication is that the shell response is sensitive to the pressure peak at the edge of the wetted surface. Since infinite peaks are not obtained during experiments, the results of this study would appear to be conservative.

Figure 8 illustrates the normal velocity of the surface of the shell relative to the center of gravity of the vehicle. These results indicate that the velocity of the shell achieves values in the order of the impact velocity. Because the pressures are computed on the basis of the velocity of a rigid moving surface, one would suspect that structural deformations may have an appreciable effect on the pressure distributions. A complete discussion of this hydroelastic interaction is given in Volume 3 of this report.

PRECEDING PAGE BLANK NOT FILMED.

### CONCLUSION

In conclusion, for the sample problem considered, it has been observed that during water impact the peak shell responses based on rigid-body pressures occur at a time appreciably before the maximum forces are applied to the shell surface. In addition, the present linear hydrodynamic theory gives a conservative result because it predicts an infinite peak pressure at the edge of the wetted surface. Finally, the high velocity of the shell surface relative to the center of gravity of the vehicle indicates that the effects of the hydroelastic interaction between the shell and the water may be of significance in the determination of the pressures and the shell responses.

PRECEDING PAGE BLANK NOT FILMED.

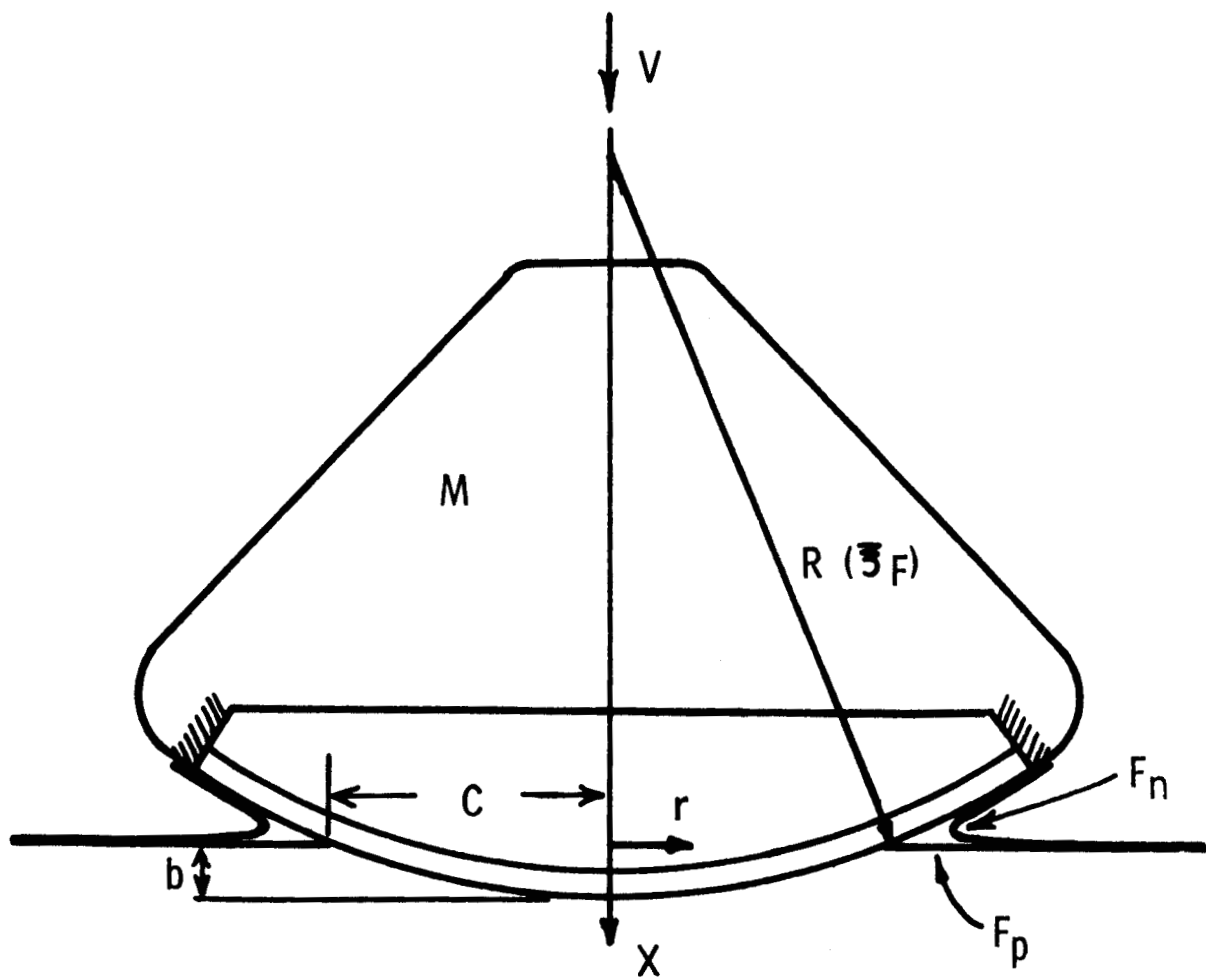


Figure 1. Model of Re-Entry Vehicle During Impact.

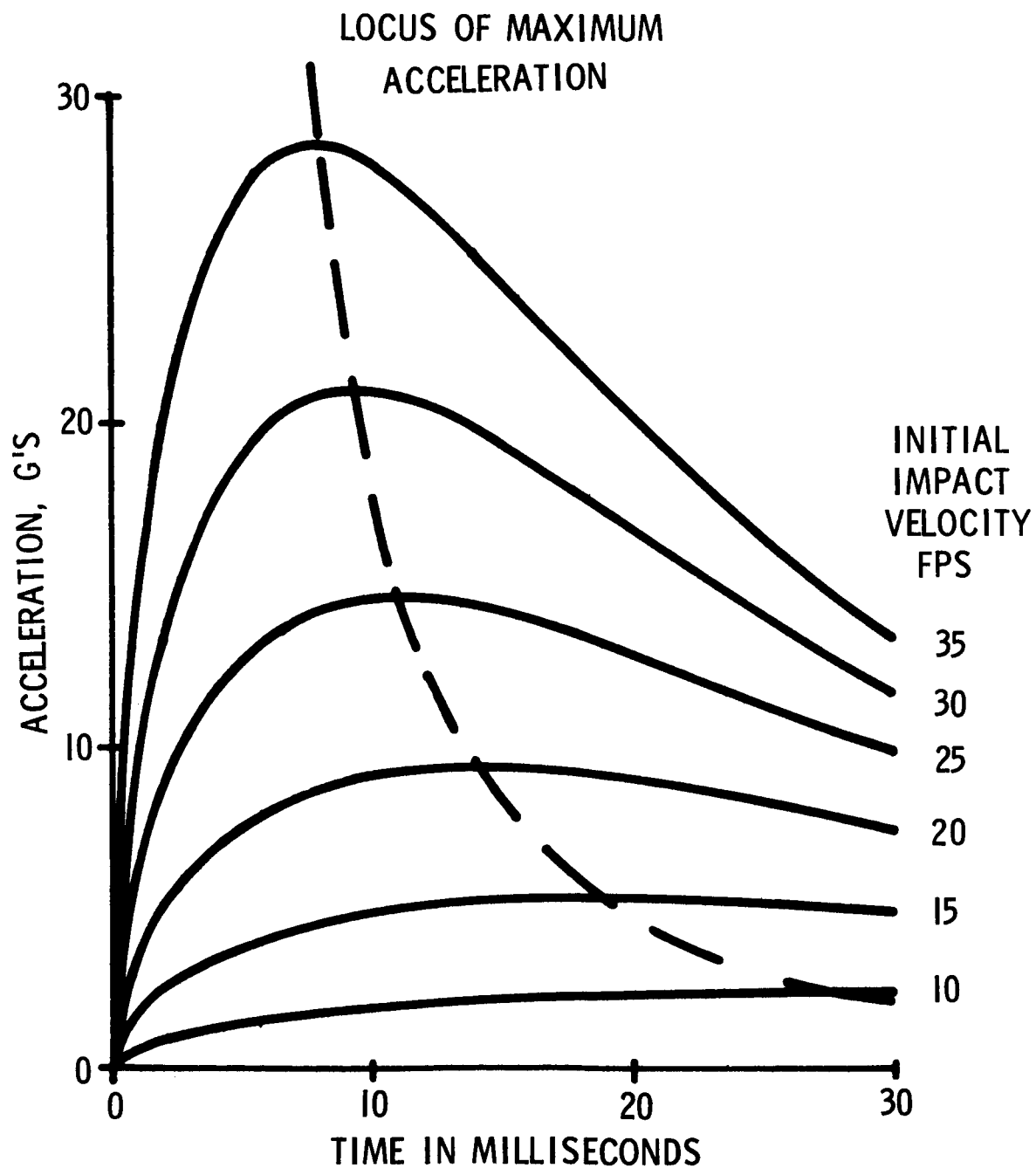


Figure 2. Acceleration of Center of Gravity of a Sphere During Impact into Water

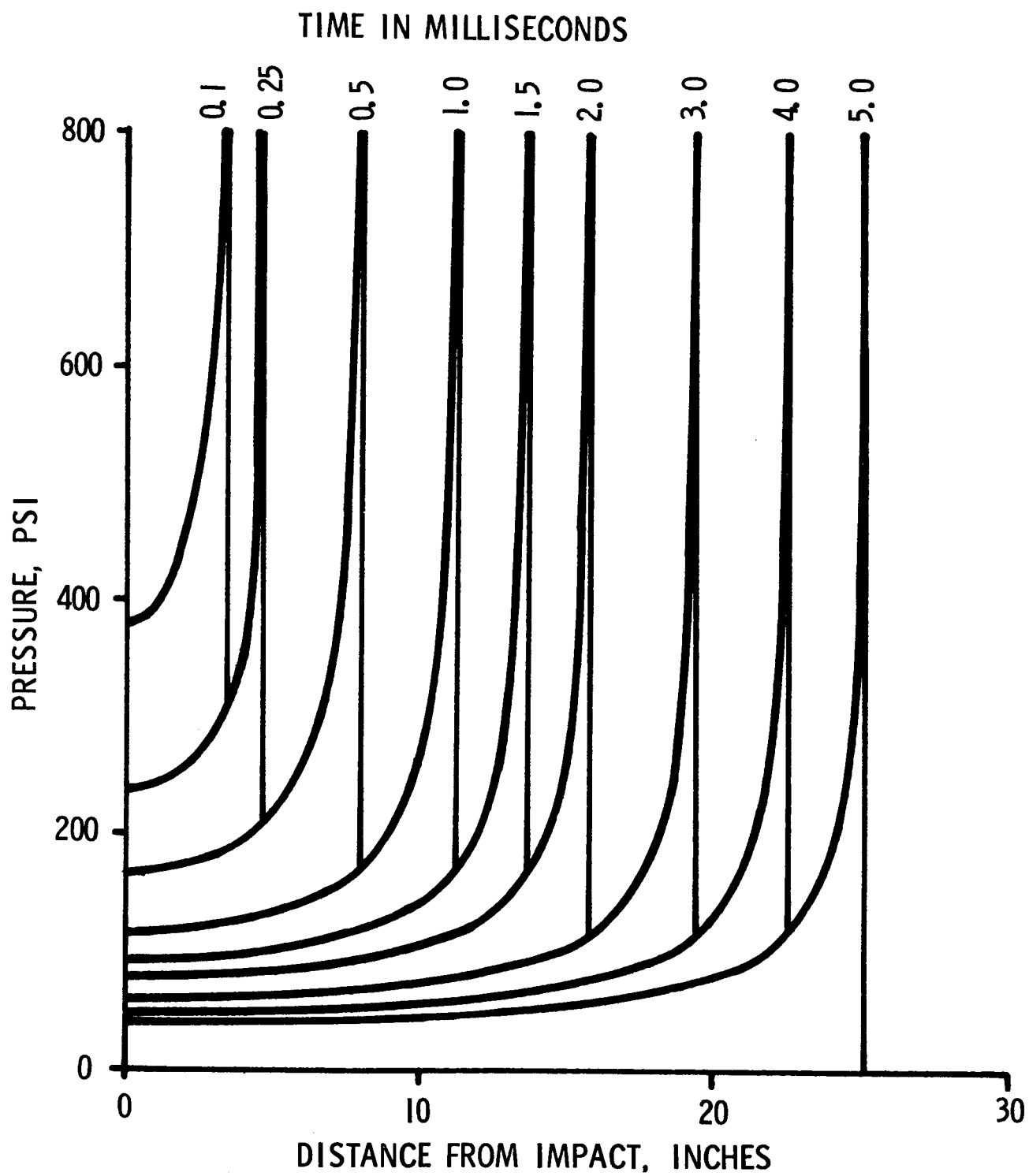


Figure 3. Pressure Profiles.



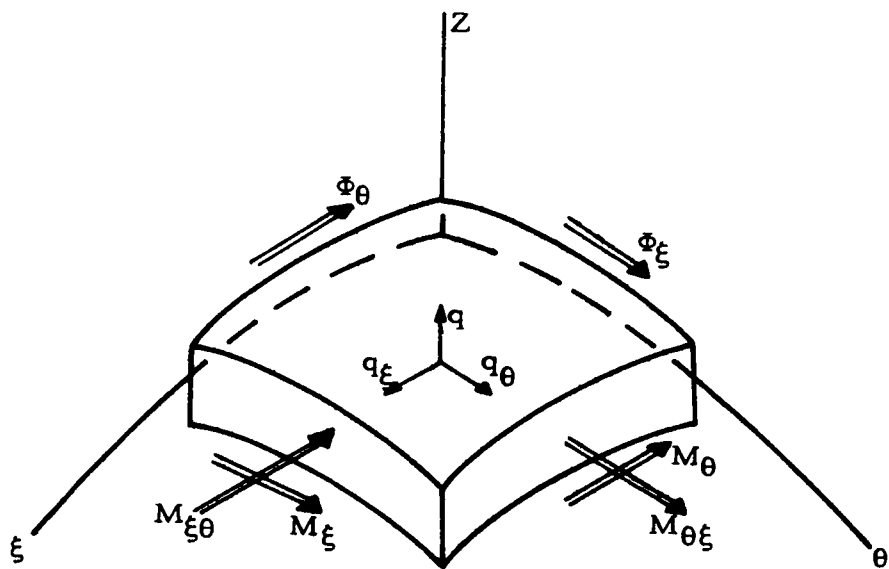
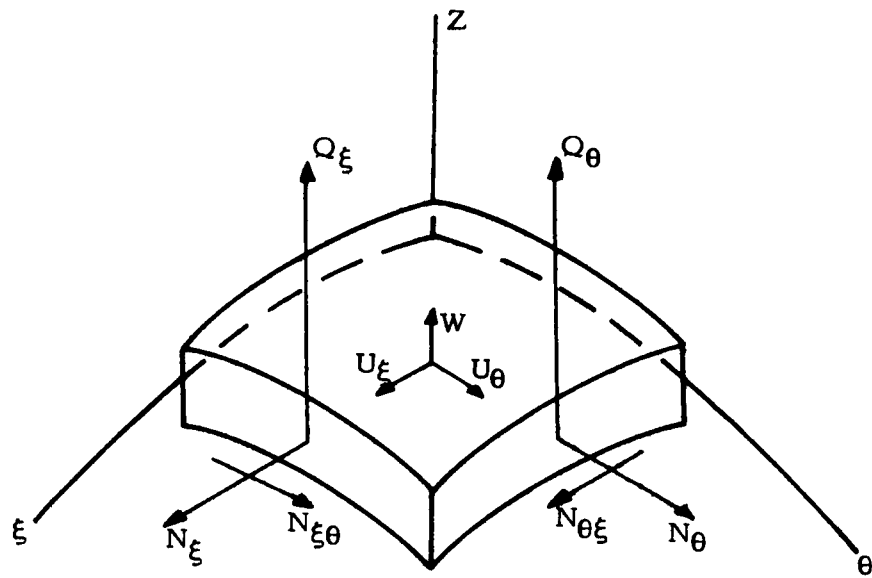
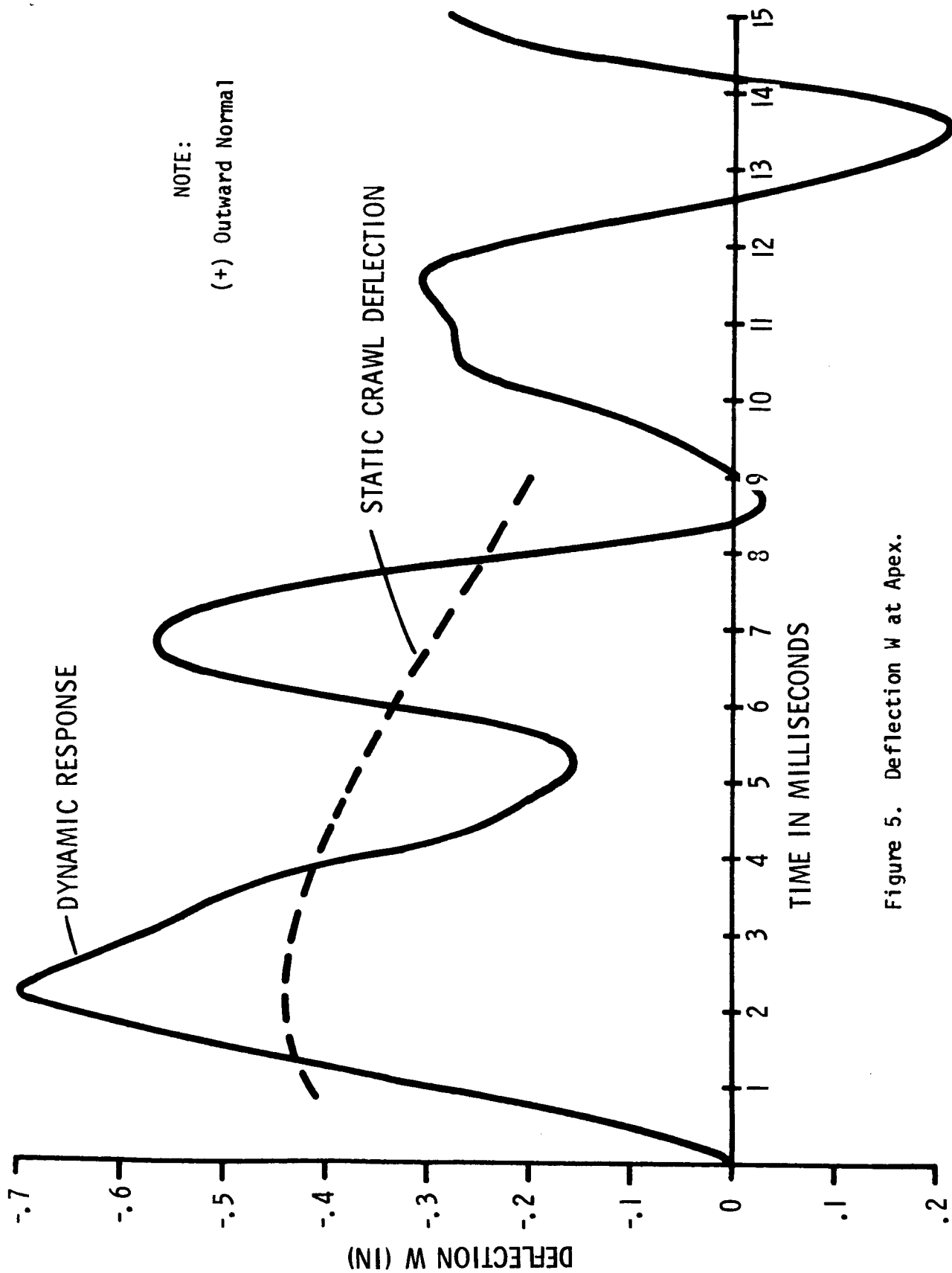


Figure 4. Shell Element.



NOTE:  
(+) Outward Normal

Figure 5. Deflection W at Apex.

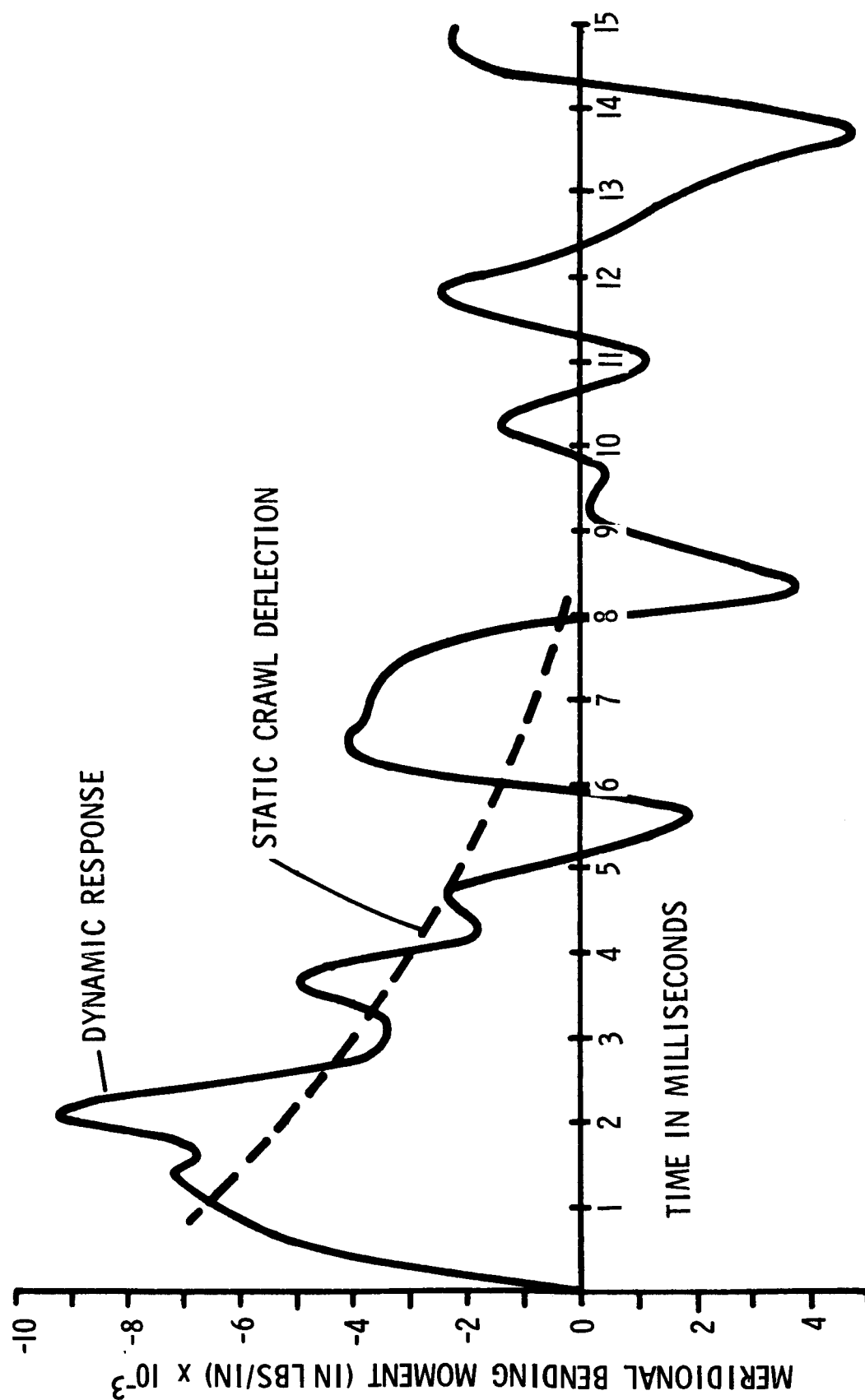


Figure 6. Meridional Bending Moment  $M_{\xi}$  at Apex.

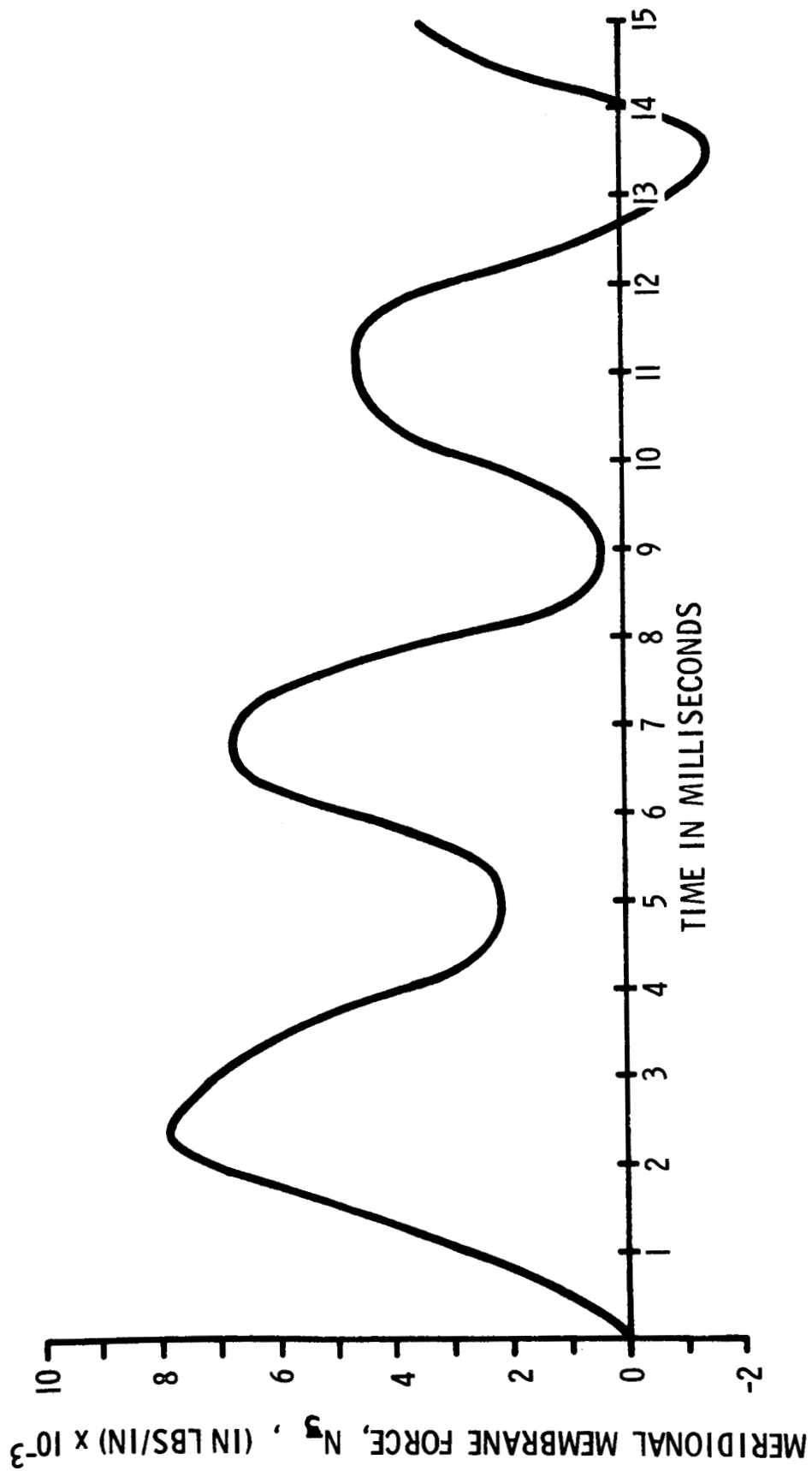


Figure 7. Meridional Membrane Force  $N_x$  at Apex.

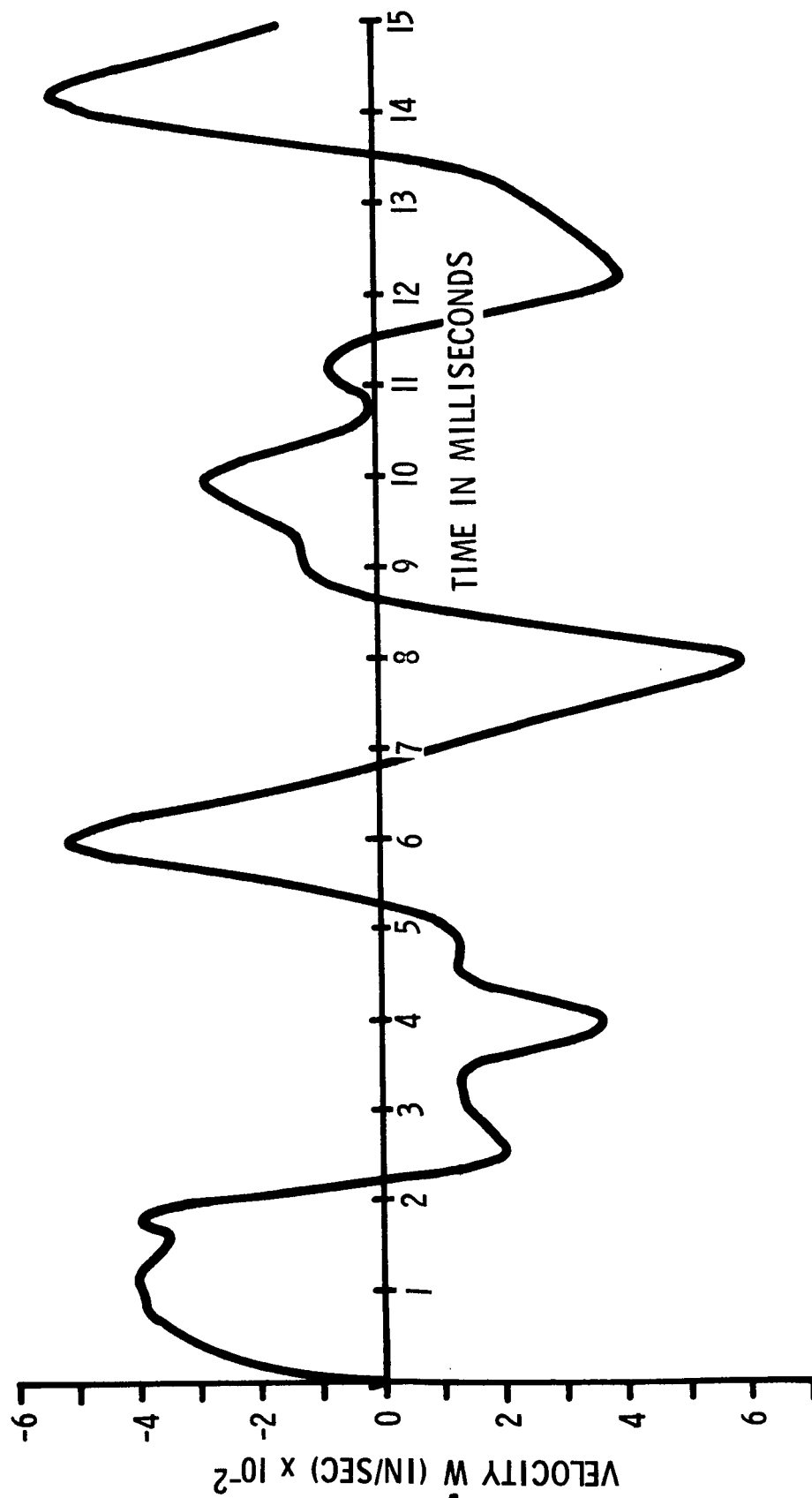


Figure 8. Velocity of Shell Apex  $\dot{w}$ .

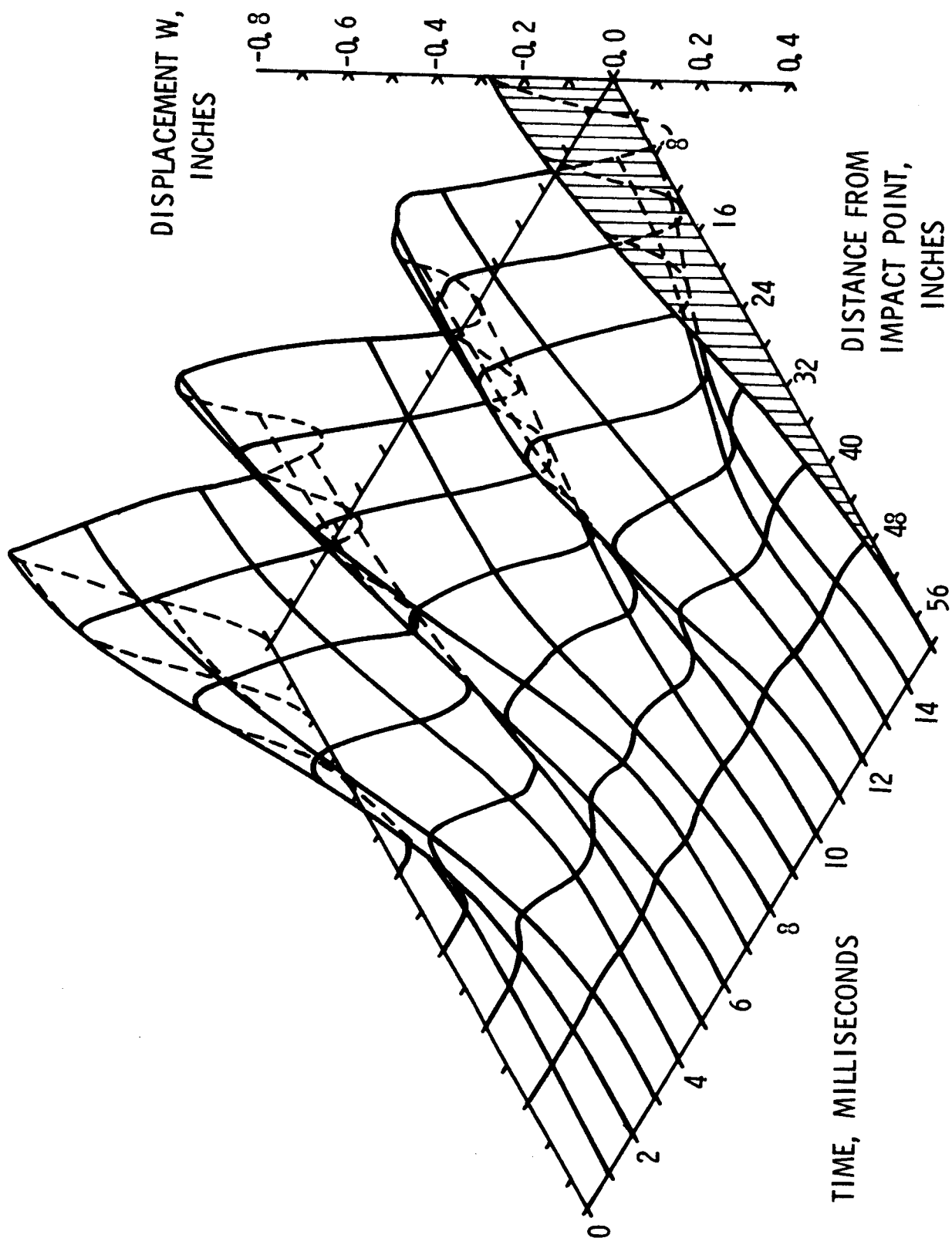


Figure 9. Deflection W.

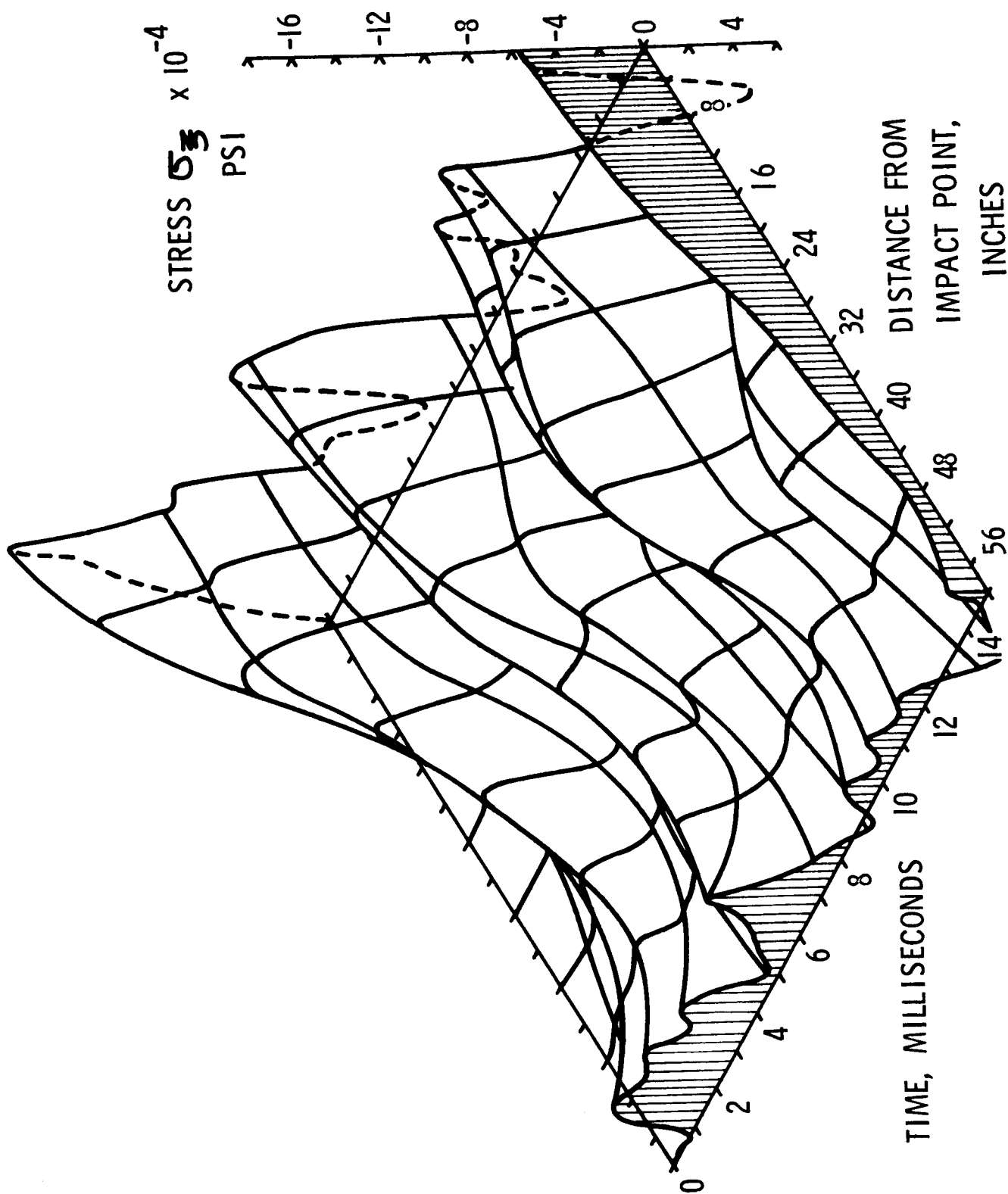


Figure 10. Meridional Stress at the Extreme Fiber.

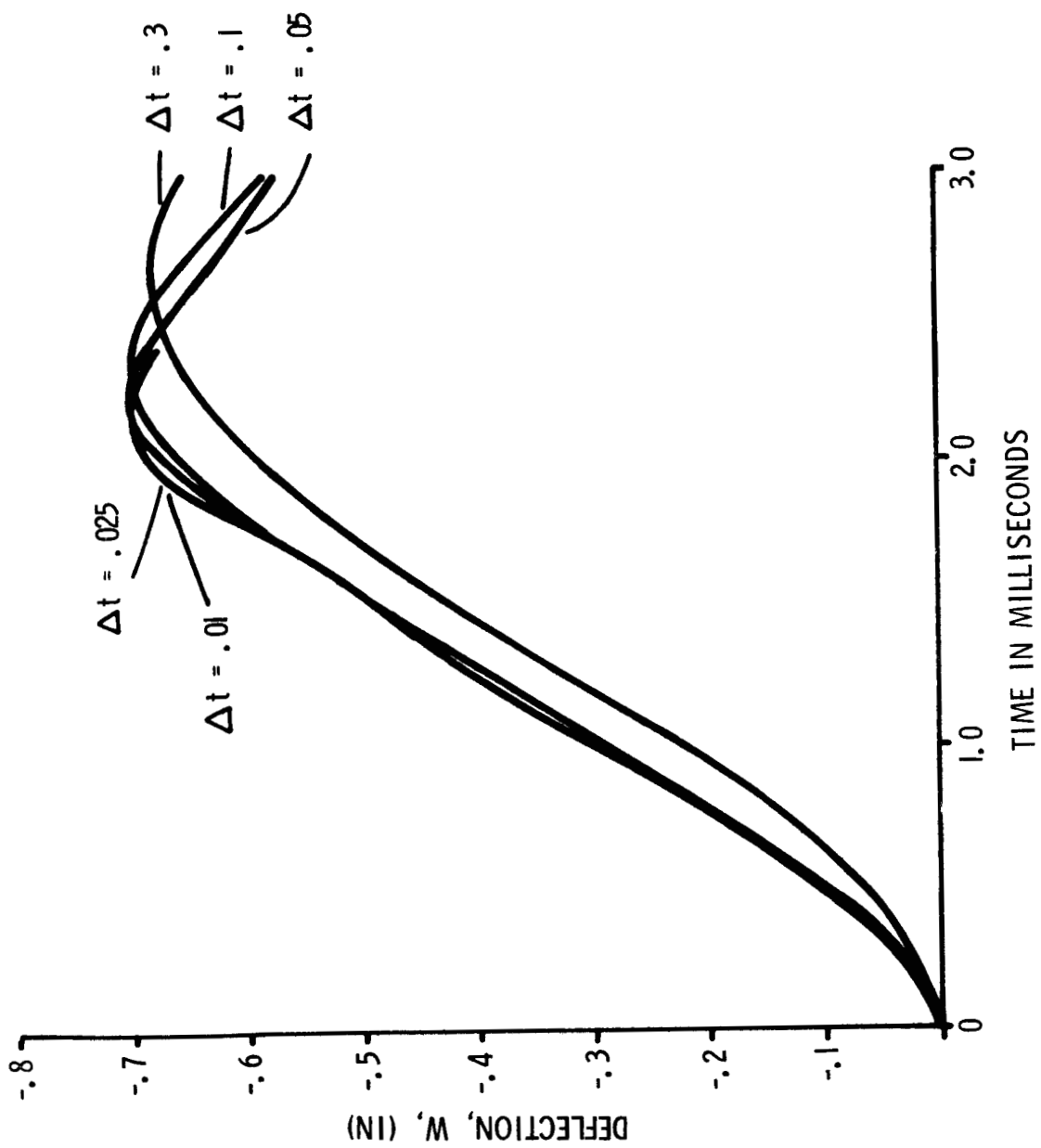


Figure 11. Deflection  $W$  at Apex for Various Time Increments.



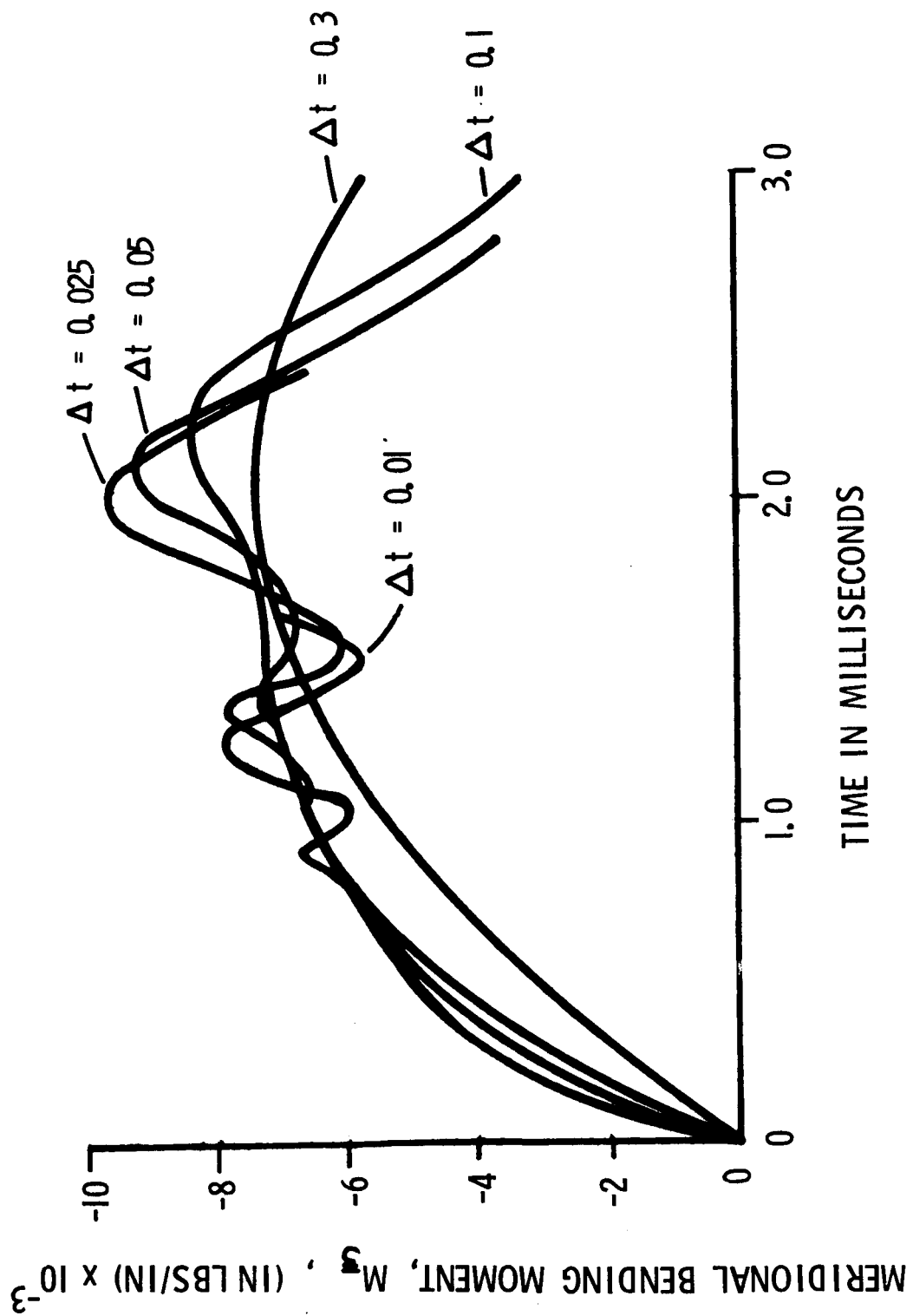


Figure 12. Meridional Bending Moment at Apex for Various Time Increments.

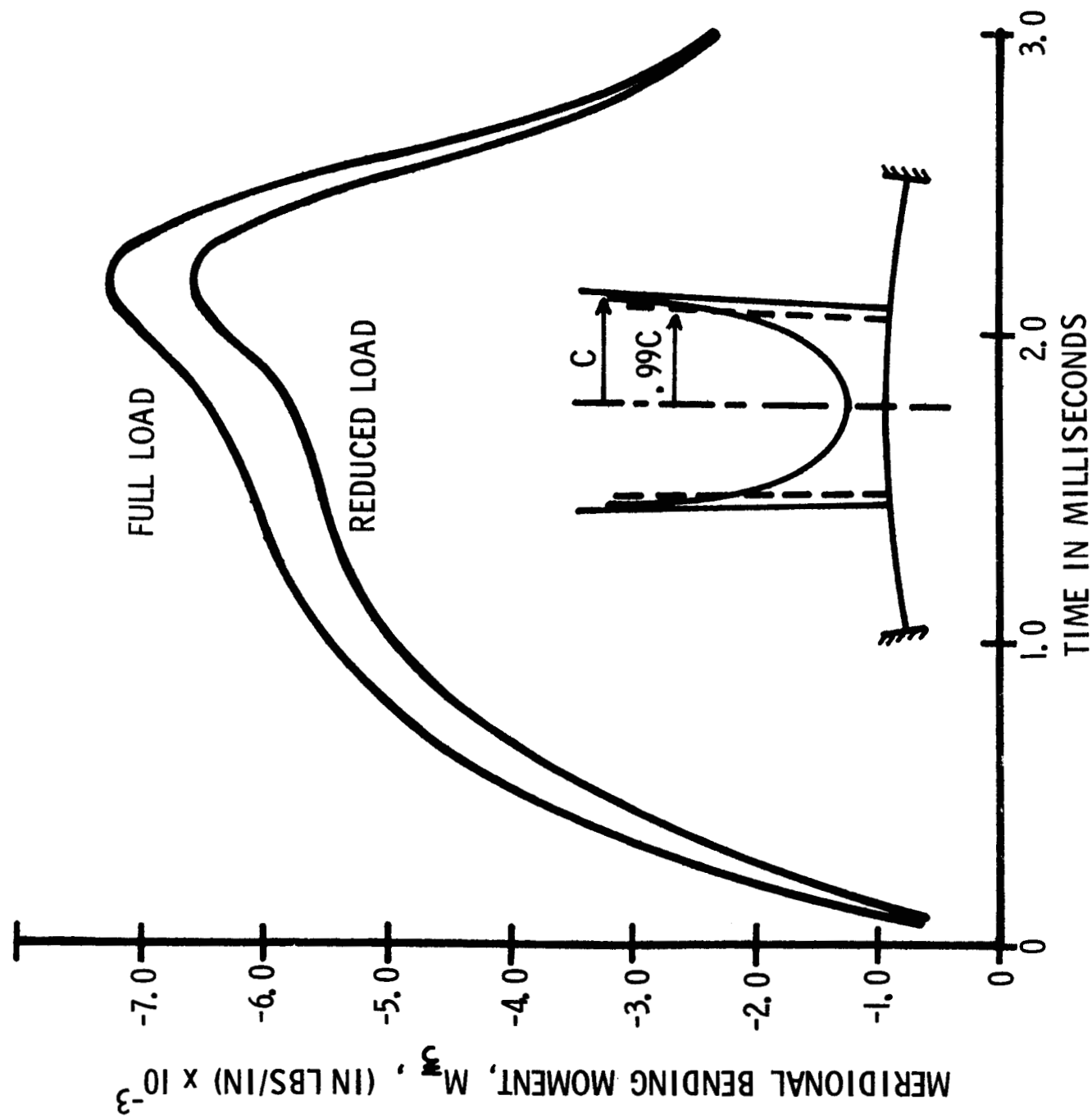


Figure 13. Reduction in Meridional Bending Moment at Apex Due To Reduced Edge Pressure.

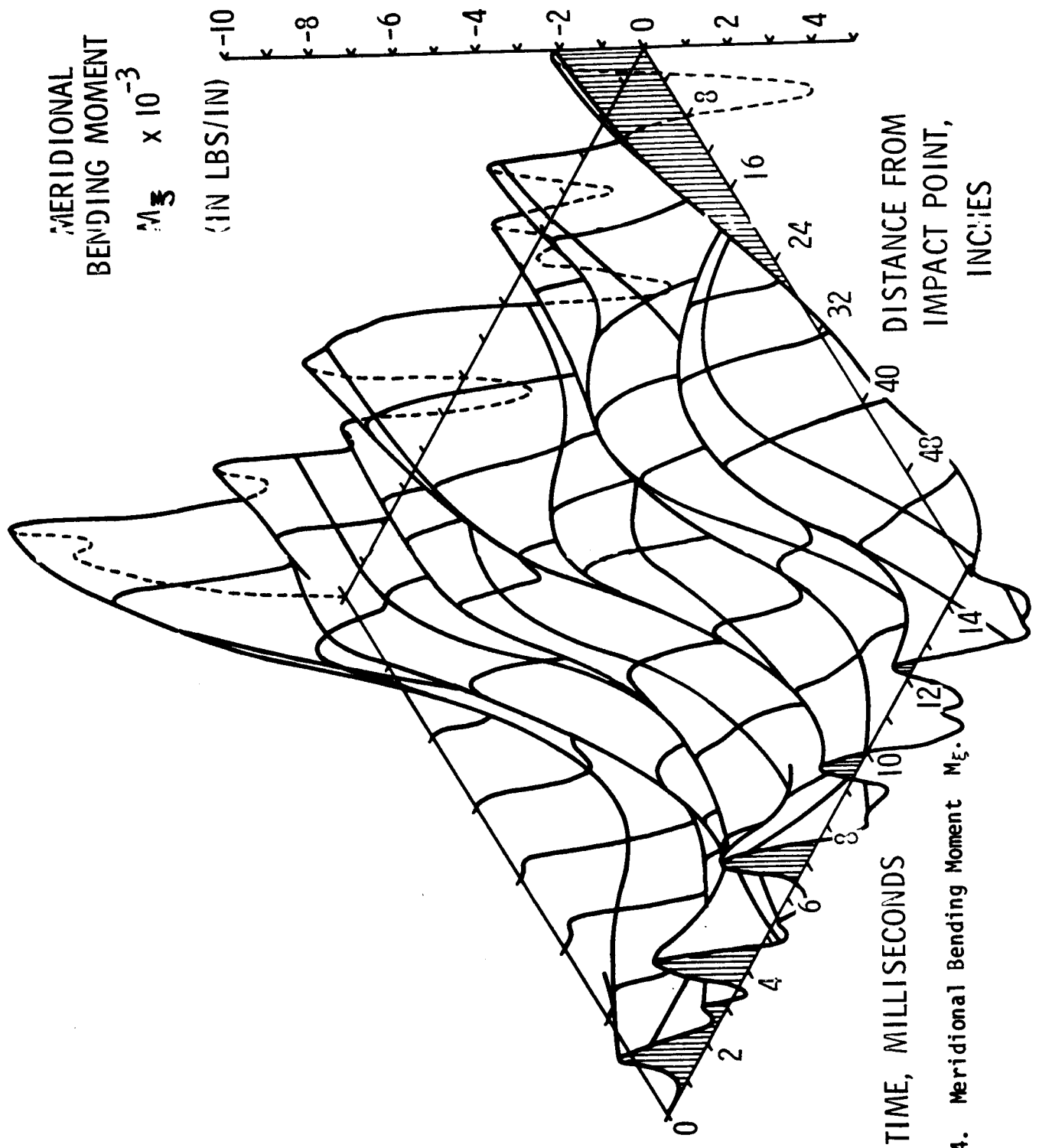


Figure 14. Meridional Bending Moment  $M_{\xi}$ .

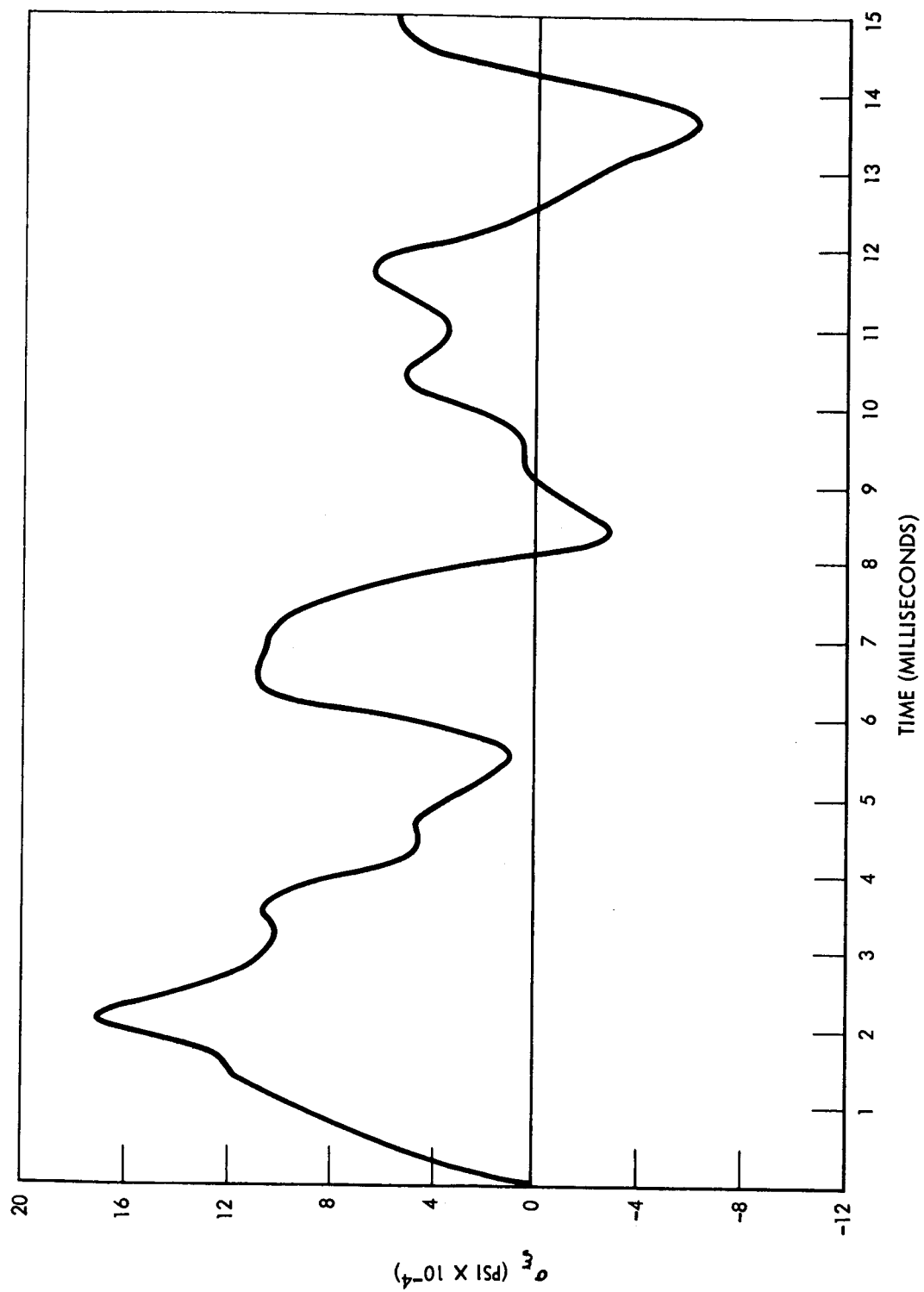


Figure 15. Stress  $\sigma_\epsilon$  On Outer Fiber at Apex.

PRECEDING PAGE BLANK NOT FILMED.

2413-02  
009 000

LEFT VIEW

RIGHT VIEW

2413-02  
010 000

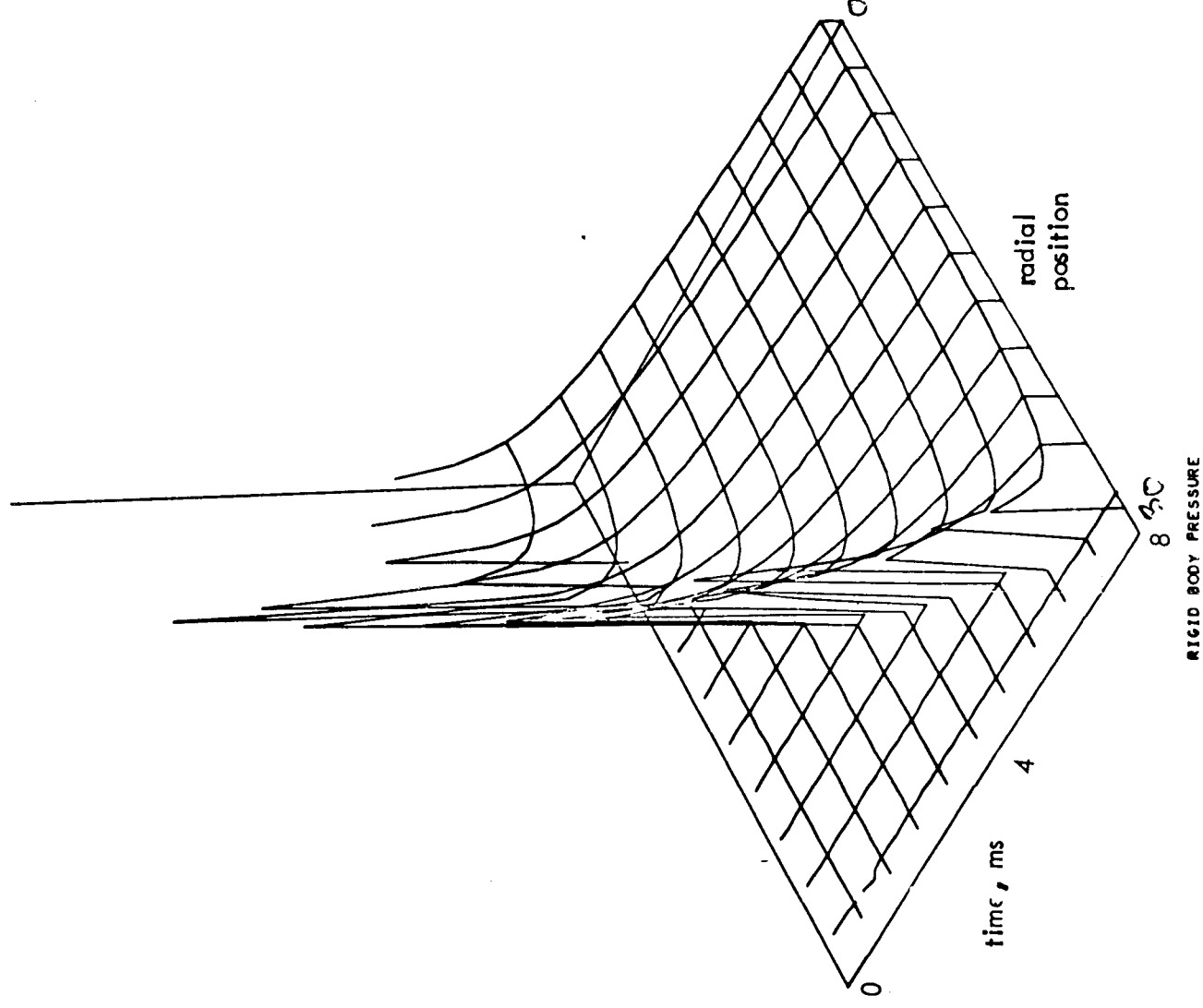
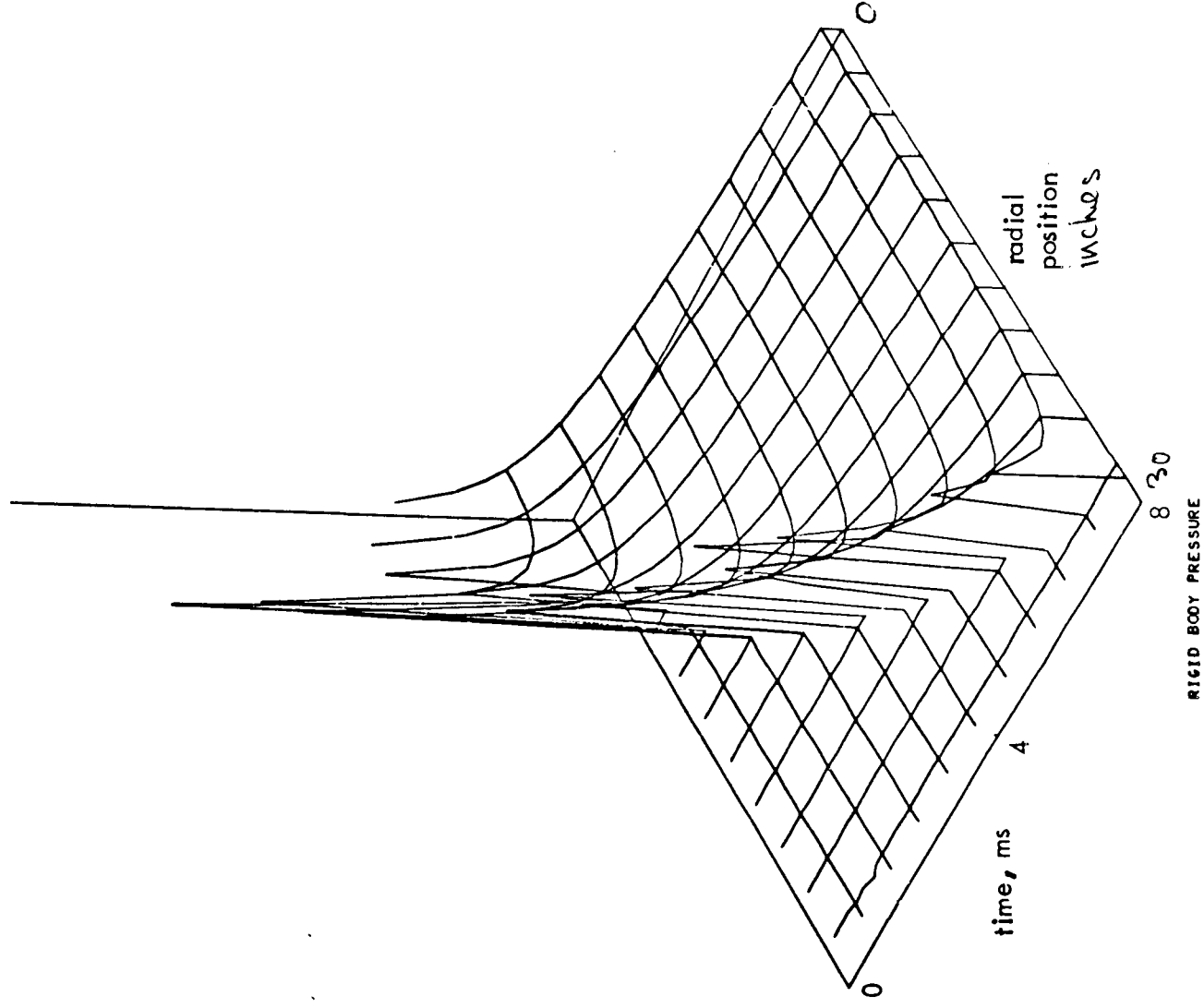


Figure 16. Stereographic Pairs of the Rigid-Body Pressures Applied to Shell.

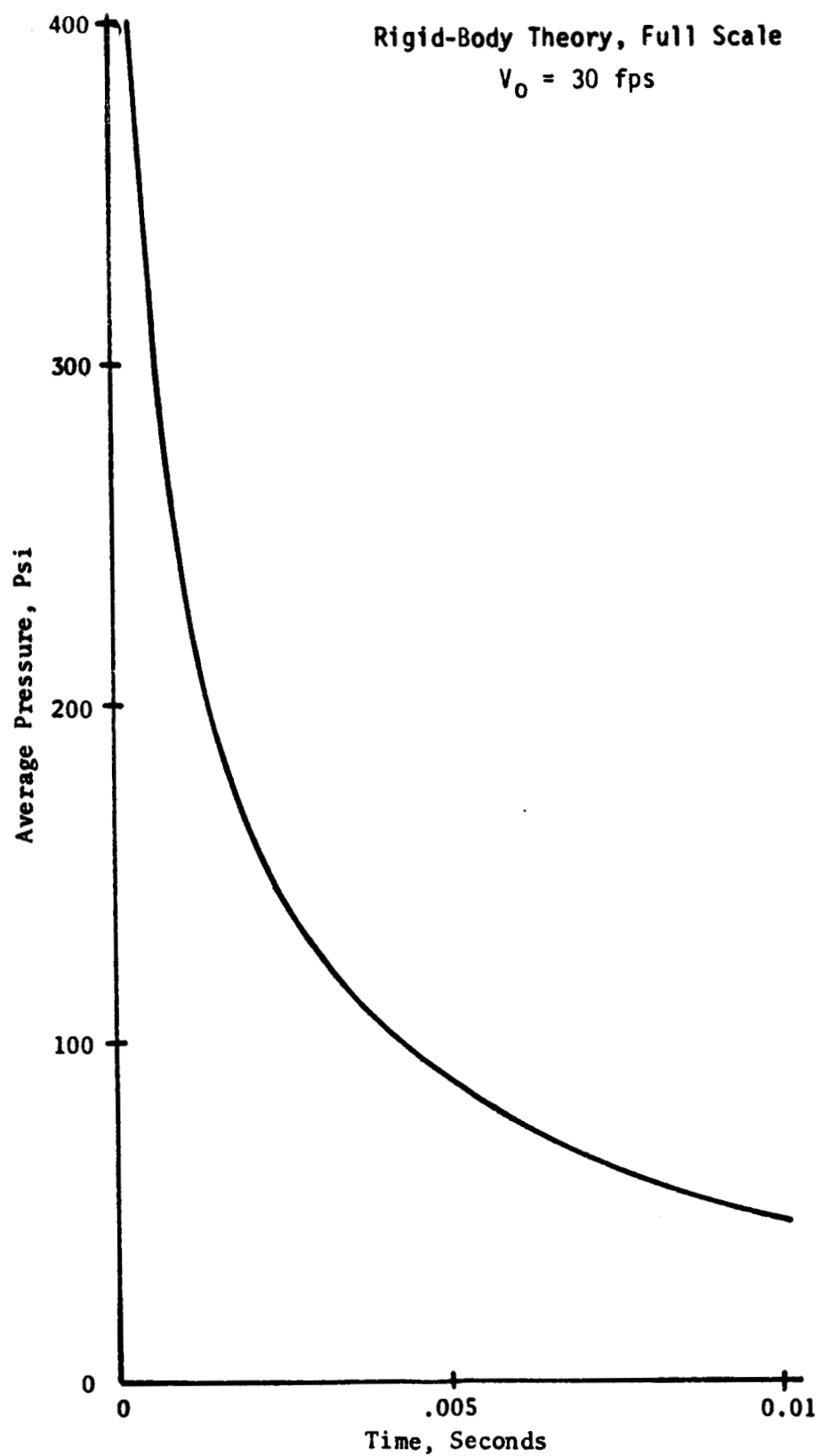


Figure 17. Average Pressure - Full Scale Model

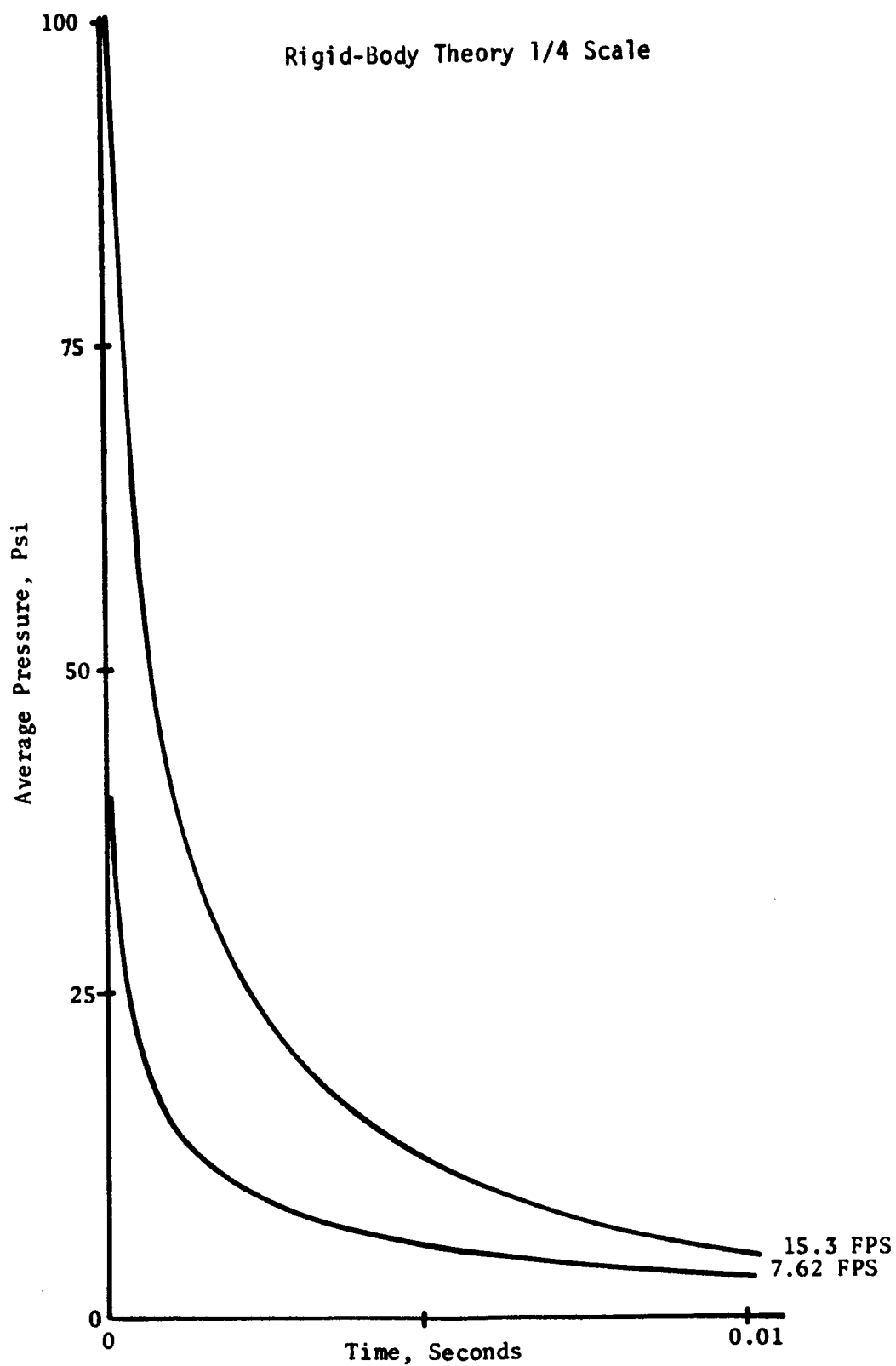


Figure 18. Average Pressure-Quarter Scale Model

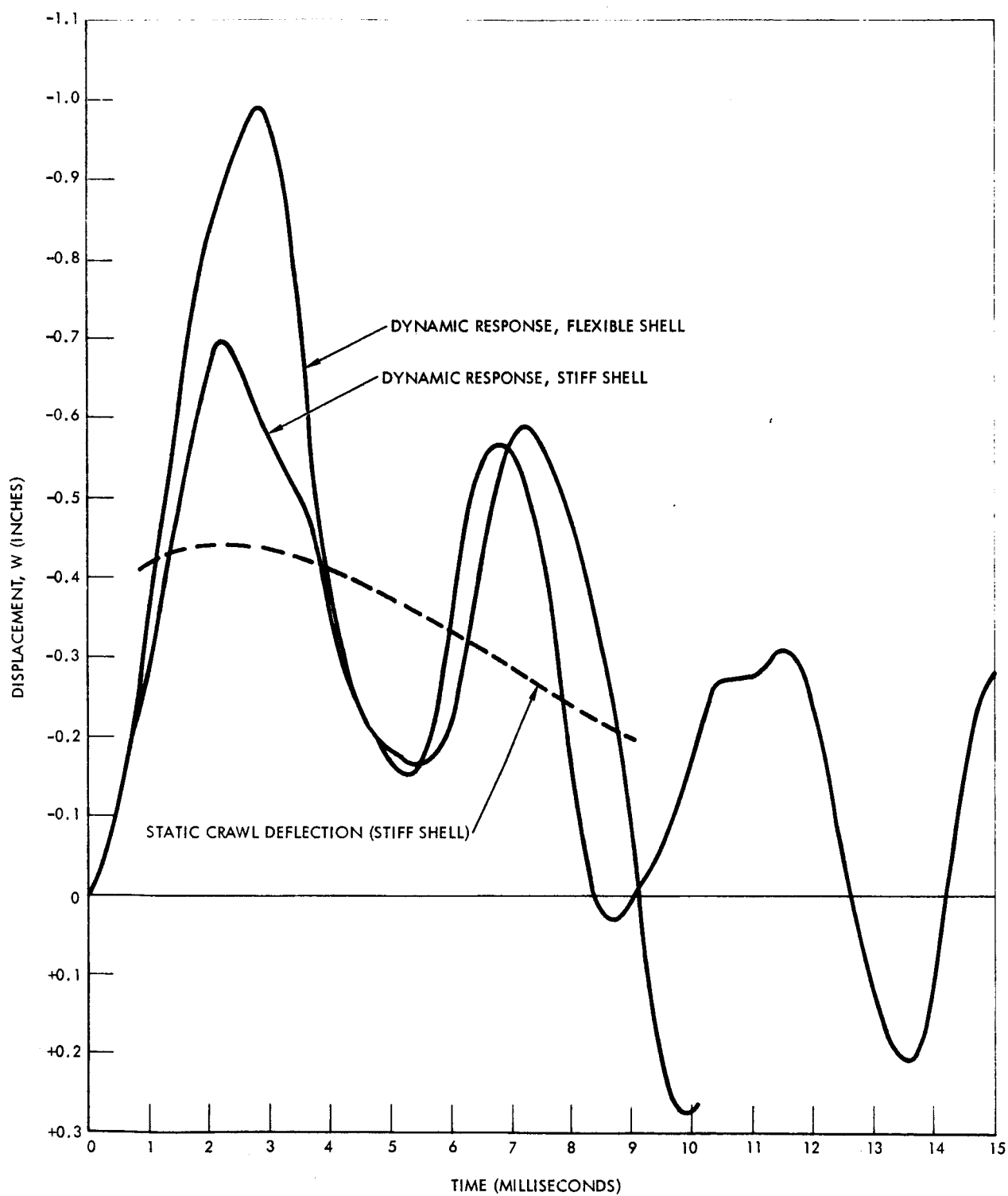


Figure 19. Displacement  $W$  at Apex Illustrating Effect of Shell Flexibility



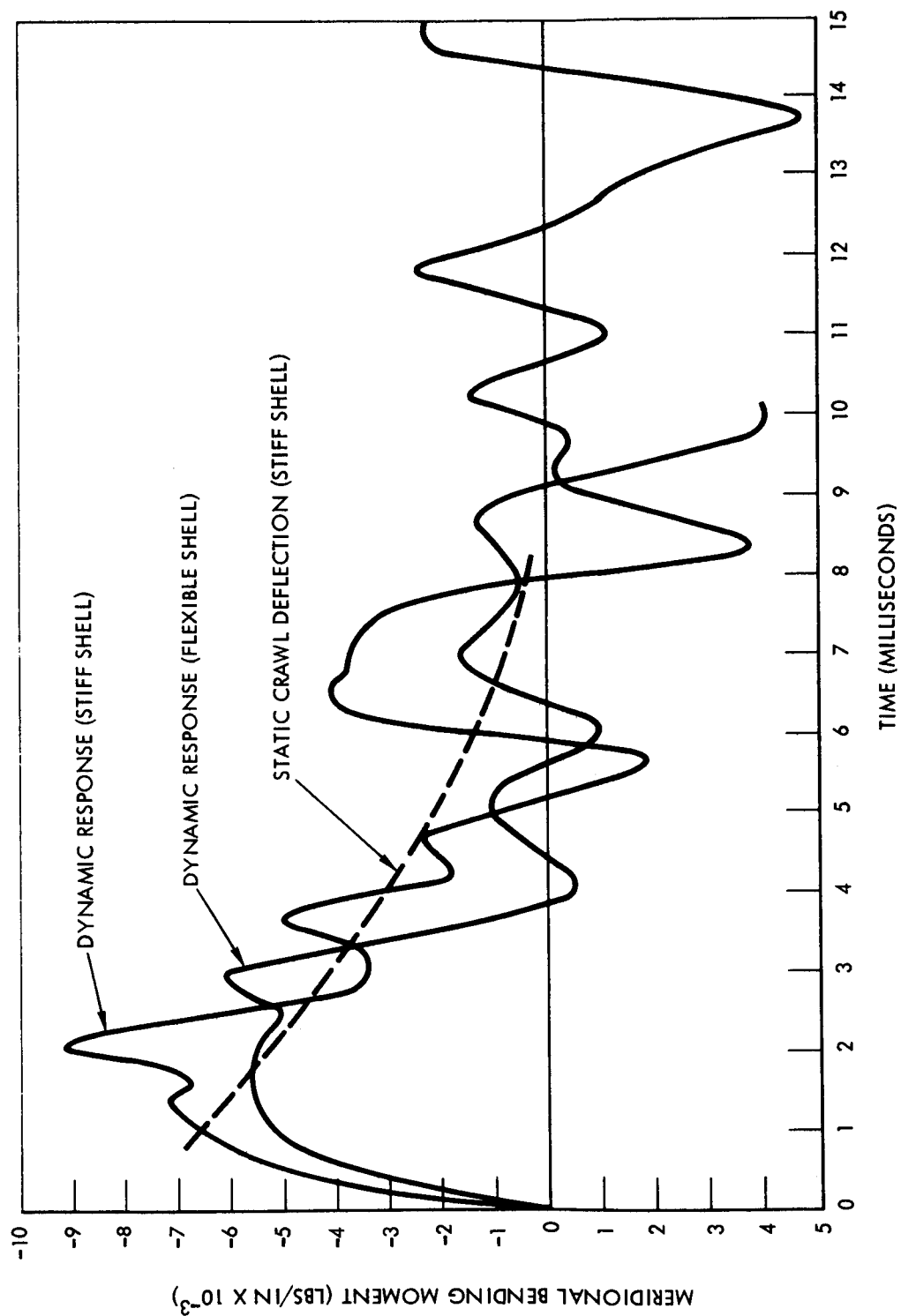


Figure 20. Meridional Bending Moment  $M_\xi$  at Apex Illustrating Effects of Shell Flexibility.

## REFERENCES

1. Sanders, J. L., Jr., "An Improved First-Approximation Theory for Thin Shells," NASA Rept. 24 (June 1959).
2. Budiansky, B., and Radkowski, P. P., "Numerical Analysis of Unsymmetric Bending of Shells of Revolution," AIAA J. 1, 1833-1842 (1963).
3. Houbolt, J. C., "A Recurrence Matrix Solution for the Dynamic Response of Elastic Aircraft," J. Aeronaut. Sci. 17, 540-550 (1950).
4. Johnson, D. E., and Greif, R., "Dynamic Response of a Cylindrical Shell: Two Numerical Methods," AIAA J. 4, 486-494 (1966).
5. Johnson, D. E., "A Proof of the Stability of the Houbolt Method," AIAA J. 4, 1450-1451 (1966).
6. Levy, S., and Kroll, W. D., "Errors Introduced by Finite Space and Time Increments in Dynamic Response Computations," Proc. 1st U.S. Nat'l Congress Appl. Mech. (A.S.M.E., New York, 1951), Vol. 1.
7. Potters, M. L., "A Matrix Method for the Solution of Second Order Difference Equations in Two Variables," Mathematisch Centrum, Amsterdam, The Netherlands, Report MR 19, 1955.
8. Chu, C. H., and Abramson, H. N., "Hydrodynamic Theories of Ship Slamming—Review and Extension," J. Ship Res. 4, 9-21 (1961).
9. Szebehely, V. G., and Ochi, M. K., "Hydrodynamic Impact and Water Entry," Applied Mechanics Surveys (Spartan Books, Washington, D. C., 1966), Eds: H. N. Abramson, H. Liebowitz, J. M. Crowley, and S. Jahasz, pp. 951-957.
10. Chuang, S. L., "Experiments on Flat-Bottom Slamming," J. Ship Res. 9, 10-17 (1966).
11. Von Kármán, T., "The Impact on Seaplane Floats During Landing," NACA TN 321 (1929).
12. Wagner, H., "Über Stoss-und Gleitvorgänge an der Oberfläche von Flüssigkeiten," ZAMM 12, 193-215 (1933).

13. Shiffman, M., and Spencer, D. C., "The Force of Impact on a Cone Striking a Water Surface," *Comm. Pure and Appl. Math.* 4, 379-417 (1951).
14. Shiffman, M., and Spencer, D. C., "The Flow of an Ideal Incompressible Fluid about a Lens," *Quart. Appl. Math.* 5, 270-388 (1947).
15. Korkegi, R. H., "Pressure Distribution on a Sphere Entering Water Based on Various Linearized-Theoretic Models," *NOTS Tech. Memo.* 808-40 (1950).
16. Lamb, "Hydrodynamics" (Dover Publications, Inc., New York, 1945), 6th ed.
17. Cappelli, A. P., "A Numerical Procedure for the Dynamic Analysis of Shells of Revolution," *Structures Technical Report 143*, Space and Information Systems Div., North American Aviation, Inc., January 1966.
18. Greenbaum, G., "Comments on Numerical Analysis of Unsymmetrical Bending of Shells of Revolution," *AIAA J.* 2, 590-591 (1964).
19. Budiansky, B., and Radkowski, P. P., "Reply by Authors to G. A. Greenbaum," *AIAA J.* 2, 595 (1964).
20. Cappelli, A. P. and Verette, R. F., "An Improved Numerical Procedure for the Solution of Shell Problems," *Structures Technical Report 141*, Space and Information Systems Div., North American Aviation, Inc., Jan. 1966.

## APPENDIX A - AUXILIARY RESULTS

In this Appendix certain auxiliary results will be presented which are complementary to the foregoing discussion (but not essential to its development).

In Figure 14 is shown the meridional bending moment  $M_\xi$  as a function of time and radial distance from the impact point. It is maximum at the apex at  $t = 2.2$  ms.

Figure 15 shows the stress  $\bar{\sigma}_\xi$  at the outer fiber of the shell apex. It is maximum at  $t = 2.2$  ms.

Figure 16 is a three dimensional schematic of the rigid-body pressures. There are two nearly identical figures here. They are the left and right views forming a stereographic pair. If an appropriate viewer is used, the pairs will fuse to yield a vivid 3-dimensional image of the pressures. We note from this drawing that the pressures decrease monotonically with time as soon as the maximum has been reached. The maximum peaks occur at the edge of the wetted surface.

Figure 17 shows the average pressure acting on the vehicle for an initial impact velocity of 30 ft/sec.

Figure 18 shows the average pressures acting on a 1/4 scale model (weight 165 lbs, radius 44.1 inches) as it impacts at 7.62 and 15.3 ft/sec.

In Figures 19 and 20 are shown the detailed effects of varying the shell flexibility. The discussion in the main portion of this volume should be referred to for further comments.